Highly variable content of fluorapatite-hosted CO32- in the Upper Cretaceous/Paleogene phosphorites (Morocco) and implications for paleodepositional conditions

Jérémie Aubineau, Fleurice Parat, Abdellatif Elghali, Otmane Raji, Aissam Addou, Clément Bonnet, Manuel Muñoz, Olivia Mauguin, Fabien Baron, Moulay Brahim Jouti, et al.

Chemical Geology xxx (xxxx) 120818

Contents lists available at ScienceDirect

Chemical Geology

journal homepage: www.elsevier.com/locate/chemgeo

Highly variable content of fluorapatite-hosted CO_3^{2-} in the Upper Cretaceous/Paleogene phosphorites (Morocco) and implications for paleodepositional conditions

Jérémie Aubineau [a,*], Fleurice Parat [a], Abdellatif Elghali [b], Otmane Raji [b], Aissam Addou [b], Clément Bonnet [a], Manuel Muñoz [a], Olivia Mauguin [a], Fabien Baron [c], Moulay Brahim Jouti [d], Oussama Khadiri Yazami [d], Jean-Louis Bodinier [a,b]

[a] Géosciences Montpellier, Université de Montpellier, CNRS UMR, 5243, Montpellier, France
[b] Mohammed VI Polytechnic University, Geology and Sustainable Mining, Ben Guerir, Morocco
[c] IC2MP Université de Poitiers, CNRS UMR, 7285, Poitiers, France
[d] OCP, Strategic Development Department, Sustainability & Green Industrial Development, Khouribga 25000, Morocco

ARTICLE INFO

Editor: Michael E. Boettcher

Keywords:
Carbonate fluorapatite
CO_3^{2-} substitutions
Paleoenvironments
Porosity
Morocco

ABSTRACT

Phosphorus (P) usually occurs as microcrystalline minerals of carbonate fluorapatite (CFA) in sediments of upwelling-related areas. The Upper Cretaceous/Paleogene marine sedimentary rocks in Morocco host the world's largest economic reserves in phosphorus, which were deposited on the eastern passive margin of the central Atlantic Ocean. However, a full petrographic, mineralogical and geochemical characterization of the Moroccan phosphate minerals is yet to be determined. Here, we use optical and scanning electron microscopies, X-ray diffraction, and infrared spectroscopy, in combination with a microprobe analyzer to document carbonate (CO_3^{2-}) substitutions in CFA from two distinct phosphate basins and their possible implications for paleoenvironmental conditions. The Moroccan phosphorus-rich deposits predominantly comprise porous phosphatic peloids and coated grains with a maximum size of 500 μm, which in turn consist of high-density nano- to micron-sized rod-shaped and sphere-like crystallites. Bulk and *in situ* analyses reveal heterogeneous CO_3^{2-} content in CFA at the regional- and grain-scale. Fourier transform infrared spectra indicate that CO_3^{2-} accommodates only in the phosphate site within the fluorapatite structure, as found in other natural phosphate minerals. Bulk CO_3^{2-} variations in CFA between phosphate basins, ranging from 1.97 to 8.24%, are likely related to depositional conditions – and thus of supersaturation with respect to CFA – during mineral formation, transport, and redeposition. Moreover, some phosphatic coated grains have revealed alternations of CO_3^{2-}-rich and CO_3^{2-}-poor CFA laminae, pointing out local differences in CO_3^{2-} concentrations in sediment pore waters. Interestingly, the change in shape and diminution in size of CFA crystallites caused by high content of CFA-hosted CO_3^{2-} could have possibly increased the intragranular porosity, highlighting an underestimated role of CO_3^{2-} on grain morphology. Considering the higher solubility of CO_3^{2-}-rich CFA than fluorapatite, the application of such phosphate rocks from specific Moroccan areas as rock phosphate powders may be of deep interest for long-term soil fertilization. These results further evidence the importance of studying phosphorites for economic, environmental, and scientific interests.

1. Introduction

Phosphorite is a marine phosphorus (P)-rich sedimentary rock containing more than 18% P_2O_5 and up to 40% P_2O_5 (Glenn et al., 1994), which constitutes the main sink for phosphate in the oceans (Ruttenberg, 2003). Phosphorus is a nonrenewable resource, but extremely important for the manufacture of fertilizers required in agriculture and chemical products. In addition to its economic value, P stimulates photosynthetic primary productivity, which, in turn, modulates ocean-atmosphere oxygen levels on geological time scales (Cox et al., 2018; Reinhard et al., 2017).

* *Corresponding author:
E-mail address: jeremie.aubineau@umontpellier.fr (J. Aubineau).

https://doi.org/10.1016/j.chemgeo.2022.120818
Received 6 January 2022; Received in revised form 7 March 2022; Accepted 15 March 2022
0009-2541/

Most of the Phanerozoic and modern phosphorite formation takes place along continental shelves underlying upwelling regimes where nutrient-rich deep waters are brought into shallow-marine coastal areas (Föllmi, 1996; Pufahl and Groat, 2016). The large flux of nutrients delivered in these settings triggers high rates of primary productivity, leading to high delivery of organic matter – and thus of P— to the sediments. Following the latter mechanism, phosphorites currently form on the western coasts of Namibia (Baturin, 2000; Compton and Bergh, 2016), Chile and Peru (Burnett, 1977; Arning et al., 2009a) as well as in the Gulf of California (Jahnke et al., 1983; Schuffert et al., 1994), and the Arabian Sea (Schenau et al., 2000). Phosphogenesis is thought to occur in the topmost centimeters of the sediment column during the earliest stage of diagenesis (Schuffert et al., 1994; Schulz and Schulz, 2005).

To understand the formation of sedimentary phosphorites, we must first consider that P is a continentally derived material sourced from the weathering of P-bearing rocks and soils (Ruttenberg, 2003). Then, rivers and groundwaters transport the solubilized phosphate anions (PO_4^{3-}) to the oceans. Upon reaching oceans, P can be assimilated into biomass and/or adsorbed onto the surface of inorganic minerals, dominantly composed of Fe/Mn-oxyhydroxides, which eventually leads to the burial of P in sediments (Ruttenberg and Berner, 1993). Once on the seafloor, remineralization of organic matter and reductive dissolution of Fe/Mn-oxyhydroxides release the organically and inorganically bound P into sediment pore waters (Cosmidis et al., 2013a). The activity of polyphosphate-accumulating microorganisms, including sulfide-oxidizing bacteria and diatoms, is also known to drive phosphogenesis by concentrating phosphates intracellularly (Diaz et al., 2008; Goldhammer et al., 2010; Schulz and Schulz, 2005). When dissolved PO_4^{3-} concentrations in interstitial waters reach supersaturation with respect to carbonate fluorapatite (CFA), P precipitates first as amorphous Ca-phosphate precursors that ultimately transform to a more stable CFA phase (Föllmi, 1996; Krajewski et al., 1994). Thus, microorganisms play a crucial role in transferring P from organic to inorganic phases where P typically undergoes a "sink-switch" (Ruttenberg and Berner, 1993). Furthermore, the newly formed primary or pristine phosphatic layers may be directly buried without experiencing post-depositional processes (Pufahl and Groat, 2016). Such fine phosphatic laminae contain low P_2O_5 concentrations, varying between 2 and 10% P_2O_5. Alternatively, the pristine phosphatic sediments undergo secondary processes like winnowing (*i.e.*, current-induced reworking agents), reworking, transport, and redeposition (Filippelli, 2011; Föllmi, 1996). These post-depositional hydrodynamic mechanisms allow phosphate minerals to concentrate in substantial amounts, promoting the formation of high-grade phosphorites with P_2O_5 contents above 18%. Hence, the formation of sedimentary phosphorites on the continental margins is a combination of different factors involving a variety of biological, chemical, and physical processes (Jahnke et al., 1983; Föllmi, 1996; Pufahl and Grimm, 2003; Schulz and Schulz, 2005; Arning et al., 2009b; Mänd et al., 2018).

The Late Cretaceous/Paleogene period is certainly one of the most important phosphogenic events in Earth's history with the emplacement of coastal upwellings that affected the South Tethyan province (Lucas and Prévôt-Lucas, 1995; Pufahl and Groat, 2016). Massive phosphate ores were, thus, deposited from North Africa to the Middle East in consequence of favorable climatic, tectonic, oceanographic, and sedimentologic factors. Specifically, Morocco hosts at least 70% of the world's known P reserves (Jasinski, 2020) that are distributed into nine phosphate basins (Fig. 1; Hollard et al., 1985). A number of studies have detailed the facies association, petrography, mineralogy, as well as inorganic and organic geochemistry of the Moroccan phosphorites (El Bamiki, 2020; El Bamiki et al., 2020, 2021; Kocsis et al., 2014, 2021; Mouflih, 2015; Nguidi et al., 2021; Prévôt, 1988; Yans et al., 2014), yet the bulk and *in situ* chemical compositions of CFA-rich inorganic particles remain poorly documented.

Apatite [$Ca_{10}(PO_4)_6(OH, F, Cl)_2$] has an extremely accommodating chemical structure leading to extensive (paired) substitutions and vacancies through the crystal lattice (*e.g.*, Nathan, 1984). The carbonate fluorapatite mineral differs from fluorapatite [$Ca_{10}(PO_4)_6F_2$] owing to the presence of carbonate anions (CO_3^{2-}) in substitution for PO_4^{3-} within the crystal lattice (Nathan, 1984). CFA mainly forms in marine environments, while pure fluorapatite often crystallizes from endogenic processes (Deer et al., 2013). Fluorine (F) 'excess' in CFA – relative to the F content in fluorapatite – could support the CO_3^{2-} substitution to maintain electroneutrality of the mineral among other cation substitutions (Knudsen and Gunter, 2002; McClellan, 1980; McClellan and Lehr, 1969; McClellan and Van Kauwenbergh, 1990, 1991; Nathan, 1984). Notably, McClellan and Lehr (1969) showed that 0.4 fluoride likely associates with one CO_3^{2-}, on average, to form CO_3F^{3-} tetrahedral groups during CO_3^{2-} substitution. Debates still persist on whether fluoride is associated with CO_3^{2-} or enters independently within the structure (Nathan, 1996; Regnier et al., 1994). A simplified structural formula for CFA was given by McClellan (1980), corresponding to $(Ca_{10-x-y}Na_xMg_y)[(PO_4)_{6-z}(CO_3)_zF_{0.4z}]F_2$. Nonetheless, this general formula does not account for vacancies in the Ca site nor other anionic substitutions like sulfate or silicate complexes. The primary CO_3^{2-} content of CFA typically ranges from 5 to 8%, which reflects the equilibrium with seawater composition during mineral formation (Nathan, 1984). This coincides with a maximum of about 1.4 to 1.5 mol of CO_2 per unit-cell in CFA (Jahnke, 1984; McClellan and Van Kauwenbergh, 1990).

Cores collected from oceanographic cruises have revealed that CFA peloids in modern unconsolidated phosphate sediments contain high porosity estimated up to 10 vol% (Lumiste et al., 2019; Mänd et al., 2018). While attempts have been made to explain the heterogeneous porosity in modern CFA particles (Mänd et al., 2018), there is no clear relationship between the chemical composition and grain porosity within CFA peloids. Carbonate substitutions in synthetic and natural apatite structure are well documented (Antonakos et al., 2007; Comodi and Liu, 2000; Jahnke, 1984; Knudsen and Gunter, 2002; McClellan, 1980; McClellan and Van Kauwenbergh, 1990, 1991; Nathan, 1984; Nathan et al., 1990; Tacker, 2008; Zwicker et al., 2021), however, the variability of such substitutions remains to be elucidated within the world's largest sedimentary phosphate deposits in Morocco. In this regard, we used X-ray diffraction (XRD), infrared spectroscopy, optical and scanning electron microscopies (SEM), and an electron microprobe analyzer (EPMA) to determine the mineralogy and chemistry of Moroccan phosphate rocks. In this study, we explore samples from two exploited phosphate basins to better understand the link between CO_3^{2-} accommodation in apatite minerals and their depositional environments. This work also aims to decipher whether CO_3^{2-} incorporation into the crystal lattice affects the grain porosity.

2. Geological background of the Moroccan phosphate series

The sedimentary successions in north- to southwestern Morocco deposited during the Late Cretaceous to Paleogene host large phosphate basins (Hollard et al., 1985), which are currently exploited. Most of the Moroccan phosphorus-bearing rocks are located in the Western Meseta and Atlas structural domains, while the Moroccan Saharan domain exclusively hosts the Oued Eddahab phosphate basin (Fig. 1). These geological zones represent the eastern passive margin of the central Atlantic Ocean, and resulted from active subsidence during central Atlantic Ocean opening in the Early Jurassic (Labails et al., 2010; Michard et al., 2008). The latter allowed thick packages of sediments to accumulate along the continental slope (Ellouz et al., 2003; Ranke et al., 1982). The Meso- and Cenozoic sedimentary cover rests unconformably on the Precambrian-Paleozoic crystalline-sedimentary base-

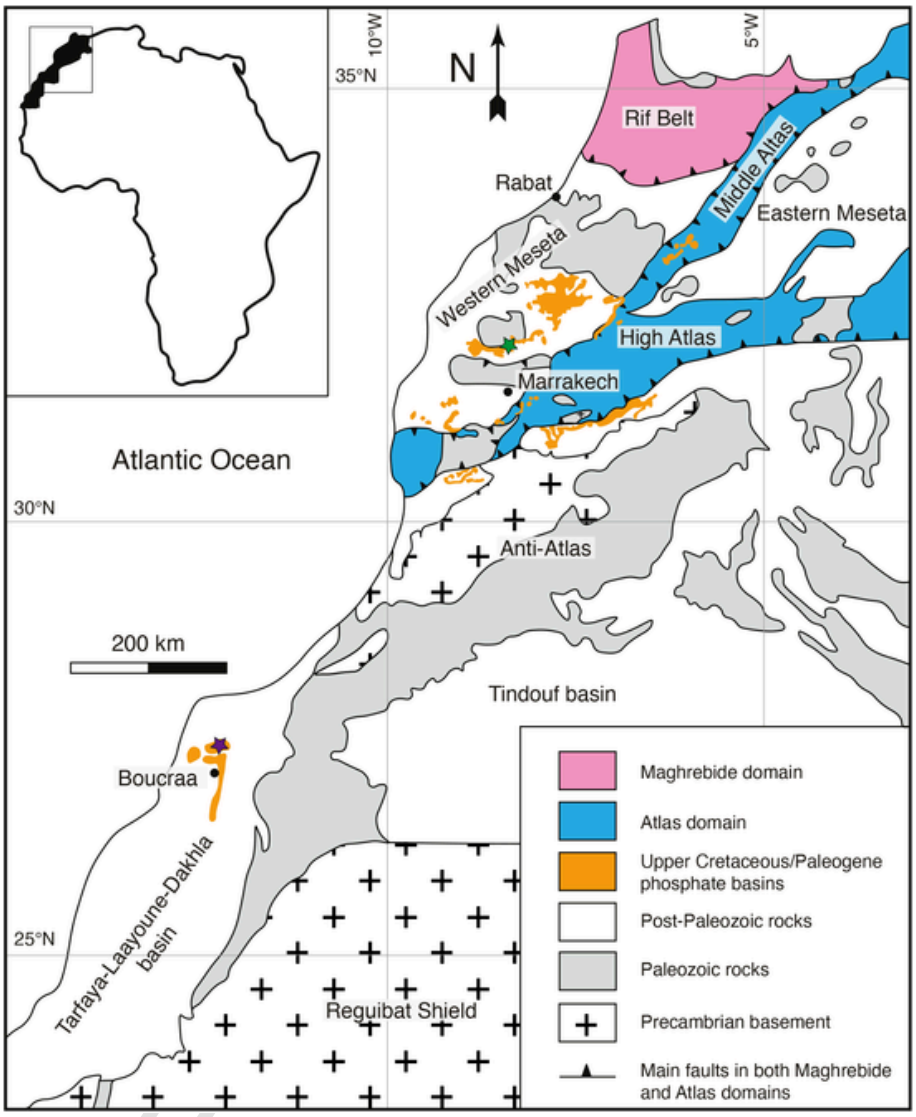

Fig. 1. Simplified geological map of Morocco highlighting the spatial distribution of the Upper Cretaceous/Paleogene phosphorites. Geological map adopted from Hollard et al. (1985). The studied samples are from the 6258 well (green star) within the Gantour basin and the 1685 well (purple star) within the Oued Eddahab basin. Structural framework and unit contours modified from El Bamiki et al. (2020). (For interpretation of the references to colour in this figure legend, the reader is referred to the web version of this article.)

ment that is overprinted by major tectonic events, including the Eburnean, Pan-African, Caledonian and Variscan orogenic cycles (Michard et al., 2008).

Synthetically, the Western Meseta block is a segment of the Moroccan Variscan belt that was generated by the closure of the Rheic Ocean and the subsequent continental collision between Gondwana and Laurussia (*e.g.*, Hoepffner et al., 2005). The deformed and metamorphosed basement is overlain by a thin tabular plateau of post-Variscan sedimentary deposits. The Atlas structural zone, comprising the elevated High Atlas and Middle Atlas Mountain belts that uplifted during the Cenozoic Alpine cycle, has recorded the highest deformation in Morocco. Such autochthonous, intracontinental belts were formed by the reactivation and inversion of Triassic fault structures that developed during the Central Atlantic rifting (Frizon de Lamotte et al., 2009; Piqué et al., 1998). In addition, the folded sedimentary cover in the Atlas domain is dominated by a km-thick Mesozoic sequence deposited due to the high thermal subsidence, while thin Cenozoic successions emplaced as subsidence lowered (Ellouz et al., 2003). The low-elevated Saharan block of South Morocco is essentially composed of the northern border of West African Craton (*i.e.*, Reguibat Shield), Anti-Atlas belt, as well as undeformed post-Paleozoic sedimentary basins, including the Tindouf basin and Tarfaya-Laayoune-Dakhla (TLD) basin (Michard et al., 2008). The TLD basin is oriented in a NE-SW direction and its infill is made of sedimentary rocks thinning eastward (Ranke et al., 1982). Specifically, the central part of TLD basin contains phosphate sediments located in the Oued Eddahab basin (*e.g.*, Nguidi et al., 2021).

The Moroccan phosphate sedimentary succession, spanning the Late Cretaceous to Eocene time (El Bamiki et al., 2020; Lucas and Prévôt-Lucas, 1995; Yans et al., 2014), is hosted by a marine-dominated sequence deposited in shallow-water environments (Chellaï et al., 1995; El Bamiki et al., 2020; Kocsis et al., 2014; Nguidi et al., 2021; Yans et al., 2014). Phosphate layers of Moroccan basins are predominantly associated with marls, limestones and dolomitic limestones. Although significant lateral facies changes occurred, the phosphate series is bracketed by over- and underlying continental deposits of Senonian and Late Eocene-Neogene ages, respectively (El Bamiki et al., 2020; Kocsis et al., 2014). The oxygen isotope composition of structural CO_3^{2-} in CFA shows variations between phosphate basins of the Western Meseta domain, which could suggest that CFA formation

took place in different depositional settings (Kocsis et al., 2014). Deeper environments thus characterize the western phosphate basins, while shallow-water coastal settings likely prevailed in the eastern border of the Western Meseta domain (Kocsis et al., 2014). In the High Atlas domain, phosphate-bearing intervals also thicken westward to more distal environments on the central Atlantic passive margin, corresponding to phosphate deposition in the outer platform (El Bamiki et al., 2020). Moreover, these phosphate-rich sediments were accumulated during second order transgressive–regressive cycles with distinguished major stratigraphic surfaces (El Bamiki et al., 2020), which helps to understand the interaction between phosphate facies and sea-level changes. However, depositional environmental conditions of phosphate-rich sediments in the Oued Eddahab basin are poorly constrained.

Although several attempts using biostratigraphic tools have been conducted to constrain the depositional age of the Moroccan phosphorites (Arambourg, 1935, 1952; Cappetta, 1981; Cappetta et al., 2014, among others; Gheerbrant et al., 1998, 2003; Noubhani and Cappetta, 1994; Ollivier-Pierre, 1982; Rauscher and Doubinger, 1982; Salvan, 1954, among others), precise ages are still unclear. These pioneering studies focused on the evolutionary aspect of vertebrates (mainly Selachian), invertebrates, dinoflagellates, and pollen faunas, rather than the stratigraphic framework. This has led to question the earlier biostratigraphic ages (*e.g.*, El Bamiki et al., 2020; Yans et al., 2014). In light of these considerations, Yans et al. (2014) conducted a high-resolution, chemostratigraphic study using isotope ratios of organic carbon ($\partial^{13}C_{org}$) in the Ouled Abdoun basin (Western Meseta domain), which allowed to refine local stratigraphy and related ages. The $\partial^{13}C_{org}$ investigation revealed the occurrence of Selandian rocks and the absence of the Upper Thanetian and Lutetian rocks in the Ouled Abdoun basin. More recently, new biostratigraphic data of calcareous nannoflora indicate that phosphate assemblages in the High Atlas region are older than previously thought, spanning the entire Paleocene (El Bamiki et al., 2020). In addition, these results have conducted to the identification of a major maximum flooding surface at the Selandian-Thanetian transition (El Bamiki et al., 2020). Combined, these new age constraints show the importance of studying the stratigraphical framework within each Moroccan phosphate domain.

3. Methods

3.1. Sampling and sample preparation

Phosphorite samples were collected from mining wells by OCP geologists in the Gantour basin (Western Meseta) close to Ben Guerir and the north part of Oued Eddahab basin near BouCrâa (Fig. 1). Ten representative samples were then selected, crushed and milled in an agate mortar without using water for bulk mineralogical analyses. Textural observations and *in situ* analyses were performed on polished thin sections that were made using standard procedures at Geoscience Montpellier, University of Montpellier, France.

3.2. X-ray diffraction

Whole-rock mineralogical composition of Moroccan phosphorites was determined by X-ray diffraction (XRD). Powdered samples were analyzed with a PANalytical X-Pert PRO MDP diffractometer using a CuKα radiation at the RRXG platform, University of Montpellier. Scan powders were recorded at 40 kV and 40 mA with an angular range of 5–65° 2θ and a step size of 0.02° 2θ per 2 s. Background subtraction, indexing of peaks and mineral identification were realized using Bruker Eva software by matching with reference XRD patterns from International Centre for Diffraction Data (ICDD) files.

3.3. Fourier transform infrared spectroscopy

Fourier transform infrared (FTIR) spectra were acquired using a Nicolet iS50 FTIR spectrometer equipped with a potassium bromide (KBr) beamsplitter and a DTGS KBr detector at the IC2MP, University of Poitiers, France. Spectra were acquired in transmission mode from KBr pellets that consist of a mixture of 1 mg of sample and 149 mg of KBr. The mixture was then pressed for 5 min at 8 kbar and dried for more than 2 h in an oven at 120 °C. An accumulation of 100 scans at a resolution of 4 cm^{-1} composes each spectrum. FTIR analyses in the 1600–400 cm^{-1} region (middle infrared – MIR) were performed to further study the bulk mineralogy of Moroccan phosphorites, especially, the CO_3^{2-} substitutions in phosphate minerals.

3.4. Microscopies

Petrographic examination of Moroccan phosphorites was carried out by optical and scanning electron microscopies at Geosciences Montpellier, University of Montpellier. Representative polished thin sections were investigated under transmitted and reflected lights using an Olympus BH2-UMA microscope combined with a Leica EC4 microscope camera. Uncoated thin sections were imaged in backscattered electron mode with a FEI Quanta 200 FEG scanning electron microscope (SEM) equipped with an Oxford Instruments energy dispersive X-ray spectrometer (EDX) at the MEA platform. Documentation of the size and morphology of CFA crystallites was performed on uncoated rock slabs in secondary electron mode. All analyses were carried out under low vacuum. Acceleration voltage, beam current, and working distance were set to 10–15 kV, 1 nA, and 10 mm, respectively.

3.5. Electron probe micro-analyzer

The concentration of major (Na, Mg, Al, Si, P, K, Ca, and Fe) and volatile (F, S, and Cl) elements in CFA grains were measured from carbon-coated thin sections using a CAMECA SX-100 electron microprobe equipped with wavelength dispersive spectrometers at Geosciences Montpellier, University of Montpellier. Point analyses ($n = 25$) were performed on non-porous areas of apatite grains. Analytical conditions of electron probe microanalyses (EPMA) operated at an acceleration voltage of 15 kV and 20 nA beam current with a ~ 1 μm focused beam in order to minimize the porosity effect. The counting time was set to 10 s for Ca, P, and Cl elements and 30 s for the others. For quantitative mapping, F, Si, P, S, Cl, K, Ca, and Fe were measured with a focused electron beam, step size of 1 μm and dwell time of 0.1 s. The detection limits are lower than 200 ppm for Mg, Al, Si, Cl, and K; lower than 400 ppm for Na, P, S, and Fe; 617 ppm for Ca and 2618 ppm for F.

The instrument was calibrated using reference material standards for each element, including albite for Na, forsterite for Mg, aluminum oxide for Al, wollastonite for Si, fluorapatite for P and Ca, orthose for K, hematite for Fe, baryte for S, and chlorapatite for Cl. Lithium fluoride (LiF) was the standard material for F analyses as it contains high content of F (73.25 wt%), which is more accurate for measuring CFA-hosted F concentrations since CFA may show a higher proportion of F than fluorapatite (McClellan, 1980; McClellan and Lehr, 1969). However, the time-dependent variability of FKα X-ray count rates during prolonged electron-beam irradiation causes analytical errors in the EPMA F measurements (Stormer et al., 1993). We observed a F migration in our fluorapatite standard and some analyzed samples, resulting in F enrichment at the sample surface (Stock et al., 2015, and reference therein). Also, F migration highly depends on the crystallographic orientation of apatite minerals, exposition of crystals to an electron beam prior EMPA analyses (*i.e.*, SEM imaging), and intrinsic vacancies within the apatite structure (Goldoff et al., 2012; Stock et al., 2015). In our analyzed samples, the F excess gave rise to unusually high F atoms per unit cell (apuc) (> 3) of CFA, which is well above the upper limit

of F incorporation (~ 2.6 F apuc) within the CFA crystal structure (McClellan, 1980; McClellan and Lehr, 1969). We, thus, removed the F excess generated by the F migration at the sample surface to enable coherent stochiometric calculations: corrected F (wt%) = measured F (wt%) – (measured F (wt%) * estimated F excess (%)). This F surplus was erratic and considered up to 30% to best fit with the known F contents in CFA (up to 4.93 wt%, McClellan and Lehr, 1969).

In addition, the CO_2 content was indirectly calculated (CO_2 = 100 – total) after the oxygen surplus of halogen atoms had been subtracted. The structural formulae of phosphate minerals were calculated using the stoichiometric model of Ketcham (2015). Assuming the complete filling of halogen site in the structure, OH content was once estimated (OH^- = 2 - F^- - Cl^-). The stoichiometric calculation is, however, difficult to constrain as Ketcham's method (2015) does not take into account large substitutions of CO_3^{2-} for PO_4^{3-} compared to apatite with any mixture of F^-, Cl^-, and OH^-. Combined, the F migration, estimated OH content, and stoichiometric model may lead to slight uncertainties in calculating the chemical formulae of apatite minerals.

4. Results

4.1. Petrography of phosphorites

The studied Moroccan phosphate rocks are predominantly composed of densely packed and unsorted phosphatic allochems that show a spheroidal to elliptical shape with a grain size ranging from 50 to 500 µm (Figs. 2, 3). The Gantour phosphorites are made of phosphatic

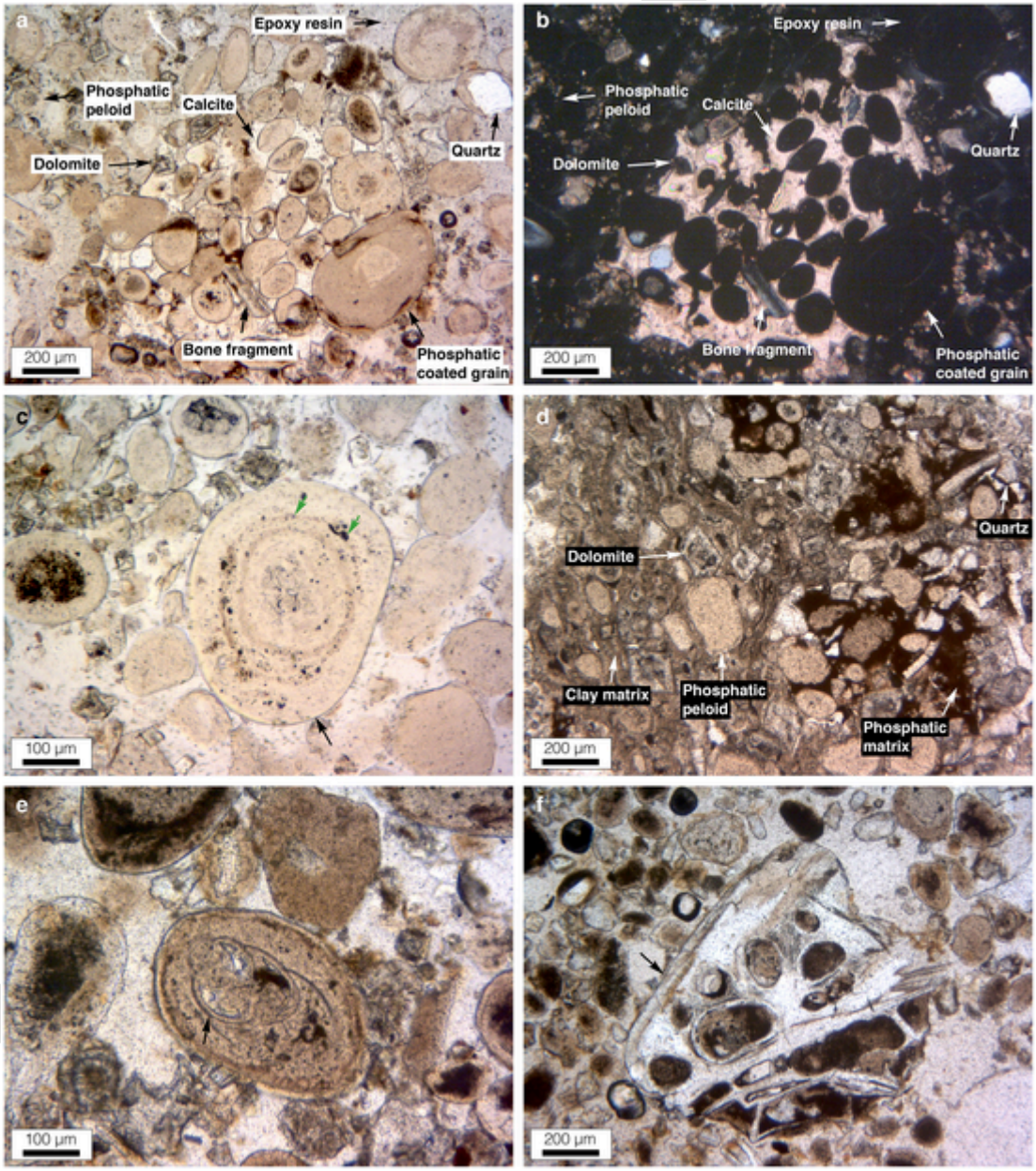

Fig. 2. Photomicrographs of representative phosphatic grains from the 6258 well, Gantour Basin. Images are in plane-polarized (**a, c-f**) and cross-polarized lights (**b**). (**a, b**) Phosphatic peloid and coated grains, bioclasts, as well as detrital quartz grains embedded within a carbonate-dominated matrix. The phosphatic allochems show a large variation in size and shape. (**c**) Phosphatic coated grain (black arrow) consisting of alternating light-brown and dark-brown laminations. Green arrows denote grain porosity. (**d**) Heterogeneous phosphatic peloids supported by dolomite as well as clay and phosphatic cements. (**e**) Phosphatized gastropod shell (black arrow) found as a nucleus within a phosphatic coated grain. (**f**) Partially phosphatized, mm-long bone fragment (black arrow). (For interpretation of the references to colour in this figure legend, the reader is referred to the web version of this article.)

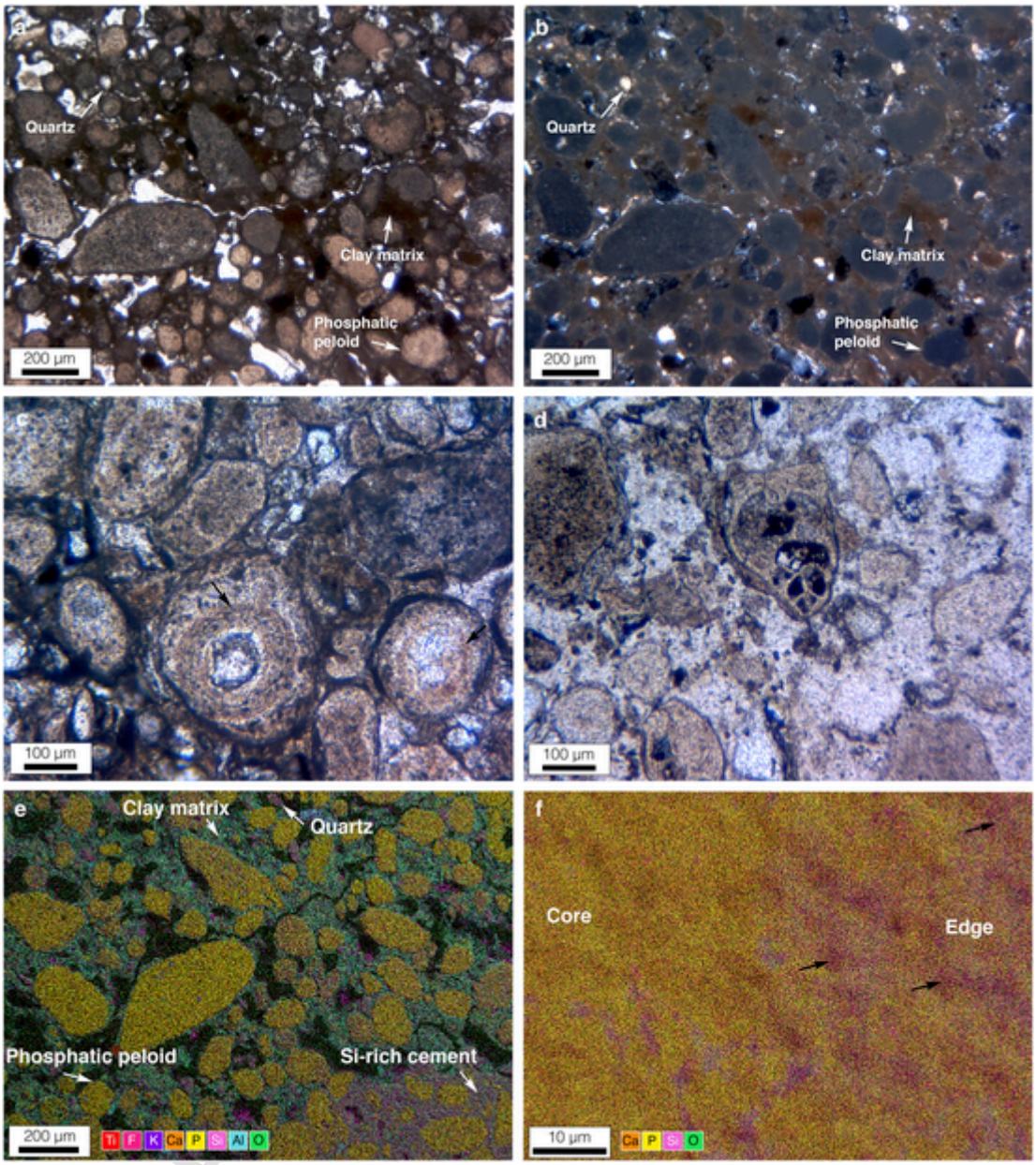

Fig. 3. Petrography with optical and scanning electron microscopes of representative phosphatic grains from the 1685 well, Oued Eddahab Basin. Images are in plane-polarized (**a, c, d**) and cross-polarized lights (**b**). (**a, b**) Phosphatic peloids and detrital quartz grains embedded within a clay matrix. The P-rich particles are heterogeneous in terms of size and shape. (**c**) Phosphatic coated grains with regular and irregular layers in thickness (black arrows). (**d**) Typical phosphatized gastropods in the observed samples. (**e, f**) Element mapping showing the occurrence of a siliceous phase that embeds particles and fills the intragranular porosity of P-rich allochems. Note the Si enrichment within the outer part of phosphatic grain (black arrow). Composite elemental maps are displayed in Figs. S1 and S2.

peloids, detrital quartz, rhombohedral dolomite, as well as coprolites and bioclasts embedded in a sparry calcite cement or clay matrix (Fig. 2). Occasionally, a P-rich matrix is present (Fig. 2d). Petrographic observations also confirmed the presence of phosphatic coated grains consisting of concentric phosphatic layers of alternating light brown and dark brown laminations (Fig. 2a, c). The laminae are either continuous and thin (< 25 µm) or discontinuous and irregular in thickness (varying from 10 to 70 µm; Fig. 2a, c). Examined grain nuclei mainly include peloids, detrital quartz, dolomite and phosphatized gastropods, while grain cortices are exclusively composed of phosphate-bearing minerals (Fig. 2a, b, e). The Gantour series also hosts numerous vertebrate bone fragments encrusted within the matrix of phosphorites (Fig. 2f). These biogenic debris are not commonly found as nuclei of phosphatic grains. Moreover, the phosphatic coated grains contain a large amount of circular black structures mostly confined to the dark brown layers, which may correspond to porous structures (Fig. 2c).

Phosphorites in the Oued Eddahab basin have different mineral and grain assemblage and petrographic characteristics compared to Gantour phosphorites with higher proportions of quartz particles and clay minerals (Fig. 3a, b). Phosphatic peloids are dominant, while phosphatic coated grains, carbonates and bone fragments are present to a lesser extent (Fig. 3c). Bioclasts in this basin are mainly represented by phosphatized gastropods (Fig. 3d). SEM-EDX examinations also display a silica-rich phase that locally occurs as cement, postdating the authigenic phosphate formation (Fig. 3e). Importantly, the phosphatic allochems in the Oued Eddahab basin show high intragranular porosity, as suggested by the presence of the Si-rich phase within peloids (Fig. 3f).

4.2. Bulk mineralogy and chemistry of phosphorites

The Moroccan phosphatic deposits were further analyzed using the XRD analytical technique. The XRD patterns of bulk samples show characteristic peaks of phosphate minerals, dolomite, calcite, quartz, opal, and clay minerals in the studied sediments (Fig. 4a, c; Fig. S3). The identification of non-basal reflections at ~4.5 Å, ~2.6 Å, and ~1.5 Å (Fig. 4a, c; Fig. S3), arising from the random stacking of swelling clay layers (Brindley, 1980), suggests that smectite likely represents the dominant clay minerals. The Gantour phosphorites have low proportions of clay minerals and Si-rich amorphous phase relative to the Oued Eddahab phosphorites, while carbonate minerals are essentially dominant in the Gantour samples. This is consistent with our petrographic observations.

Bulk mineralogy reveals that carbonate fluorapatite is the main phosphate mineral, which is characterized by (211), (112), and (300) strong diffraction peaks in the 2.82 to 2.68 Å region (Fig. 4a, c; Fig. S4, Brown, 1980; Jahnke, 1984). Extensive substitutions are known in the sedimentary apatite mineral group. Specifically, the substitution of CO_3^{2-} for PO_4^{3-} results in a slight shift of the (211) and (300) strong reflections towards lower spacing values with occasionally an overlapping of (211) and (112) peaks (Brown, 1980; Jahnke, 1984; LeGeros et al., 1967; LeGeros, 1981). The studied bulk XRD profiles thus indicate the presence of CO_3^{2-}-rich fluorapatites in the Gantour phosphorites and CO_3^{2-}-poor fluorapatites in the Oued Eddahab phosphorites (Fig.

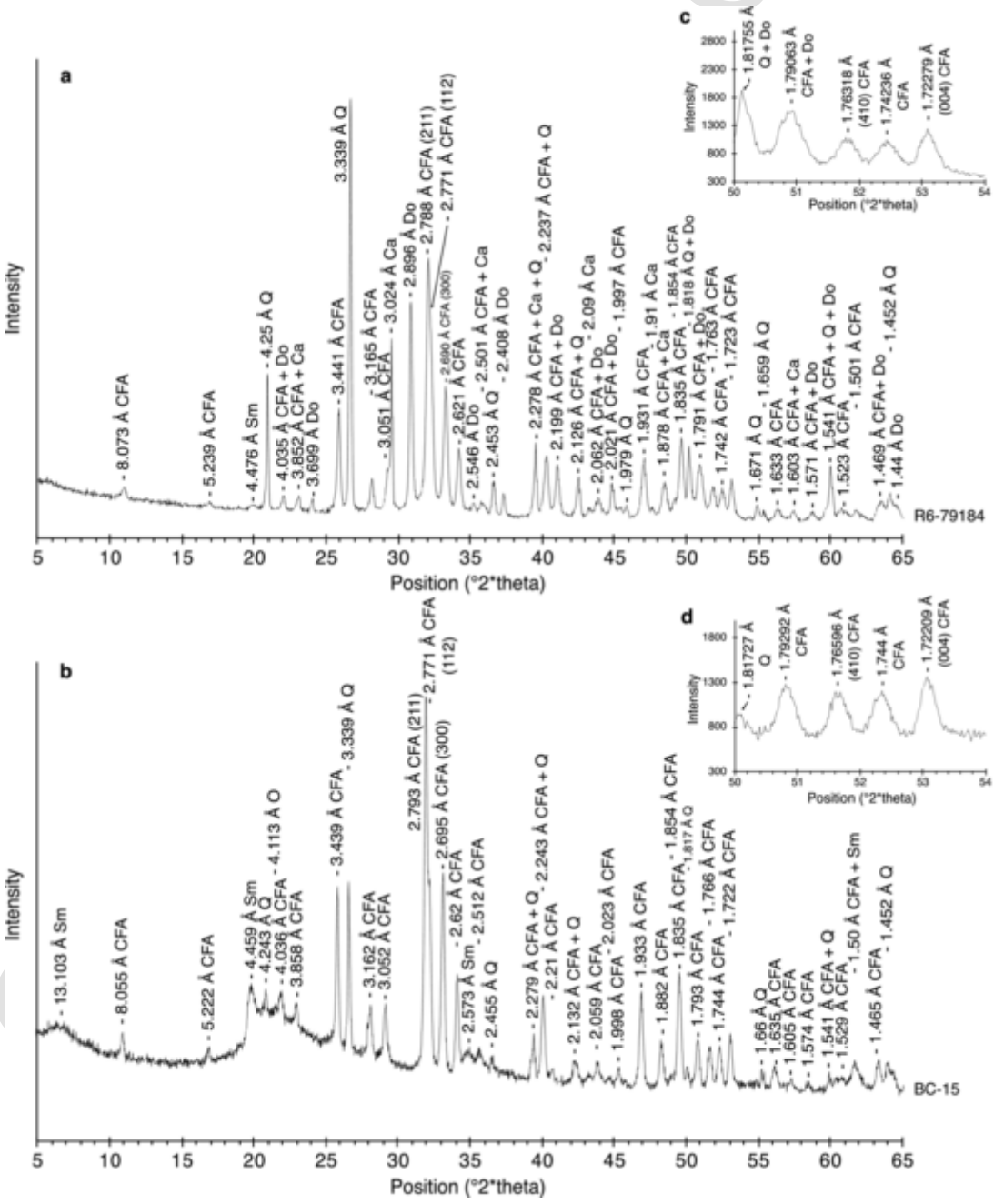

Fig. 4. XRD patterns of randomly oriented bulk powders of Moroccan samples from the 6258 (**a, b**) and 1685 (**c, d**) wells. (**a, c**) Representative phosphorites showing the main mineralogical phases. (**b, d**) Close-up of (410) and (004) reflections allowing the determination of CO_3^{2-} content in phosphate minerals. Note the absence of dolomite overlap for the CO_3^{2-} measurement.
Calcite (Ca); carbonate fluorapatite (CFA); dolomite (Do); opal (O); quartz (Q); smectite (Sm).

4a, c; Figs. S3, S4). In addition, measurement of CO_3^{2-} content in CFA can be achieved using specific XRD reflections (Gulbrandsen, 1971; Schuffert et al., 1990). Schuffert et al. (1990) introduced an empirical equation between the concentration of CO_3^{2-} and the difference in °2θ (Δ2θ) of the (004) and (410) CFA peaks. The estimated standard error of CFA-hosted CO_3^{2-} content is less than 0.5%, which makes this method reliable. The mean CO_3^{2-} content of Gantour CFA is 7.42 ± 0.74% (1σ, n = 5), more than twice the average CO_3^{2-} content of 3.34 ± 0.90% (1σ, n = 5) in the Oued Eddahab CFA (Table 1; Fig. 4b, d; Fig. S5). Although it was suggested that this method was unreliable in the presence of dolomite (Schuffert et al., 1990), our XRD patterns do not show any overlap of the (410),(004) pair reflections of CFA with diffraction peaks of dolomite (Fig. 4b, d). Intensity of CFA reflections in the 1.77 to 1.72 Å region does not vary between each basin compared to the peaks in the 1.82 to 1.79 Å area.

FTIR analyses of the bulk fraction in both Gantour and Oued Eddahab samples were essentially performed to elucidate the structural position of CO_3^{2-} substitution in CFA (*e.g.*, Madupalli et al., 2017). The MIR spectra for both lithologies are presented in Fig. 5. First, they show the four fundamental internal vibrations of PO_4^{3-} at 964 cm^{-1} ($\nu1$), 473 cm^{-1} ($\nu2$), 1041 and 1093 cm^{-1} ($\nu3$), and 568, 578, and 604 cm^{-1} ($\nu4$) (Antonakos et al., 2007; Comodi and Liu, 2000; Madejová et al., 2011). The two bands at 525 and 913 cm^{-1} may be indicative of silicate substitution for PO_4^{3-} (Comodi et al., 1999). Alternatively, the Si-O-Al bending vibration in the 520 cm^{-1} region is typical of Al-rich smectite and the Al_2-OH bending band, appearing at 915 cm^{-1}, is a characteristic of some Al-containing clays (Farmer, 1974; Madejová et al., 2011). Moreover, the absorption bands at 714, 876, and 1430 cm^{-1} in the Gantour phosphorites are diagnostic of calcite (Fig. 5a; Farmer, 1974; Madejová et al., 2011). The weak band at 729 cm^{-1} is likely a feature of dolomite in the Gantour phosphorites (Fig. 5a), while the doublet at 776 and 797 cm^{-1} is assigned to quartz in the Oued Eddahab samples (Fig. 5b).

The diagnostic bands for CO_3^{2-} in phosphate minerals are localized in the 860–890 cm^{-1} ($\nu2$; out-of-plane bending vibration) and 1400–1600 cm^{-1} spectral regions ($\nu3$; asymmetric stretching vibration) (Antonakos et al., 2007; Comodi and Liu, 2000; Elliott, 2002; Fleet, 2009; LeGeros et al., 1969; Madupalli et al., 2017; Regnier et al., 1994; Tacker, 2008). The $\nu2$ CO_3^{2-} bands of apatite minerals are, however, difficult to assess due to the strong overlap with calcite absorption bands. It has been established that CO_3^{2-} can accommodate in two sites of the apatite structure, including the hydroxyl site within the channels along c-axis (defined as A-type substitution) and PO_4^{3-} tetrahedron (defined as B-type substitution) (Tacker, 2008, and reference therein). The MIR spectra of our studied samples show a primarily B-type CO_3^{2-} substitution characterized by absorption bands near 873, 1430, and 1454 cm^{-1}, compared to those of A-type CO_3^{2-} substitution at about 879, 1465, 1530 cm^{-1} (Fig. 5; Regnier et al., 1994; Tacker, 2008; Madupalli et al., 2017). Furthermore, additional bands near 866 cm^{-1} and a broad shoulder at ~1470–1500 cm^{-1} may reveal the occurrence of surface labile CO_3^{2-} (*i.e.*, not integrated into the crystal lattice) (Deymier et al., 2017). Compared to the 1454 cm^{-1} band, the 1430 cm^{-1} band in the Gantour phosphorites has a higher absorbance than in the Oued Eddahab phosphorites, which can be assigned to the asymmetric stretching vibration of calcite in this spectral region. The overall decreasing intensity of the CO_3^{2-} absorption bands in the Oued Eddahab samples indicates the decreasing content of CFA-hosted CO_3^{2-} (Fig. 5), consistent with the XRD data.

4.3. Elemental composition of CFA in the Moroccan phosphorites

Electron microprobe analyses of phosphatic peloids and coated grains show distinct chemical compositions between the Gantour and Oued Eddahab samples (Table 2). The CaO compositions average 53.73 ± 0.63% (1σ, n = 10) and 53.65 ± 0.60% (1σ, n = 15) for the Gantour and Oued Eddahab phosphatic grains, respectively. Elevated contents of CO_2, averaging 6.86 ± 0.73%, characterize the Gantour phosphatic grains, while CO_2 contents of Oued Eddahab phosphatic particles are five times lower, with a mean of 1.17 ± 1.16%. In the Gantour CFA, the increasing CO_2 contents are accompanied by decreasing P_2O_5 contents and increasing MgO, Na_2O, and SO_2 contents. Specifically, the P_2O_5 mean for the Gantour phosphatic allochems is 34.70 ± 0.92%, while that for Oued Eddahab P-rich particles is higher, with a mean of 39.59 ± 1.17%. The average MgO, Na_2O, and SO_2 concentrations of CFA differ between the two Moroccan basins by up to 0.22, 0.41, and 0.51%, respectively. Moreover, F content is relatively uniform at ~4.2 ± 0.2 wt% in the Moroccan CFA. The Al_2O_3, FeO, K_2O, and Cl contents are either very low or negligible in all the studied samples. Finally, the Oued Eddahab phosphatic grains host SiO_2 contents as high as 2.66%, while those in Gantour do not exceed 0.94%.

The average structural formula of Gantour phosphates ($Ca_{9.34}$ $Na_{0.19}$ $Mg_{0.07}$) [$(PO_4)_{4.8}$ $(CO_3)_{1.54}$ $(SO_4)_{0.13}$ $(SiO_4)_{0.06}$] ($F_{2.18}$, $Cl_{0.01}$, $OH_{0.02}$) (n = 10, with traces of Al, Fe, and, K) confirms the presence of CO_3^{2-}-rich CFA, while the Oued Eddahab phosphatic grains have a chemical composition close to the end-member fluorapatite, with a general formula ($Ca_{9.71}$ $Na_{0.07}$ $Mg_{0.02}$) [$(PO_4)_{5.58}$ $(CO_3)_{0.37}$ $(SO_4)_{0.05}$ $(SiO_4)_{0.19}$] ($F_{2.19}$, $Cl_{0.01}$) (n = 15, with traces of Al, Fe, and, K). The complete EPMA dataset of structural formulae is given in Table 3. These results corroborate the substitution of CO_3^{2-} for PO_4^{3-}, the upper limit of about 1.5 mol of CO_2 in the CFA structure and the presence of vacancies in the Ca site. The F migration leads to the lack of accurate F measurements, which does not allow us to comment on any relationship between F and CO_2 contents nor F excess within the crystallographic CFA structure.

4.4. The sedimentary CFA grains

Under SEM, the Gantour phosphatic peloids are commonly rounded and slightly elongated with smooth surfaces (Fig. 6a-d). The latter are

Table 1
Positions of (410) and (004) XRD reflections and estimated CO_3^{2-} content (%) for the studied Moroccan phosphorites. Carbonate concentration (%) in CFA is calculated as $10.643x \times {}^{2} - 52.512x + 56.986$ where x stands for $\Delta2\theta_{(004-410)}$ (Schuffert et al., 1990).

Area	Well	Level	Sample	(410) Å	(004) Å	(410) °2θ	(004) °2θ	Δ2θ	CO_3^{2-} content
Gantour Basin	6258	SA3S	R6–13	1.76347	1.72279	51.801	53.119	1.318	6.27
		DSP1	R6–30	1.76249	1.7232	51.832	53.105	1.273	7.38
		DSP1	R6–29	1.76195	1.72324	51.849	53.104	1.255	7.86
		C2S	R6–25	1.7618	1.72354	51.854	53.094	1.240	8.24
		C2M	R6–79184	1.76278	1.72344	51.823	53.097	1.274	7.35
Oued Eddahab Basin	1685	C1S	BC-16	1.76903	1.72383	51.626	53.084	1.458	3.05
		C1S	BC-15	1.76596	1.72209	51.723	53.142	1.419	3.89
		C1IB	BC-12	1.76539	1.72216	51.740	53.140	1.399	4.35
		C2S	BC-9	1.76814	1.72350	51.654	53.095	1.441	3.42
		C3S	BC-6	1.76876	1.72202	51.635	53.144	1.510	1.97

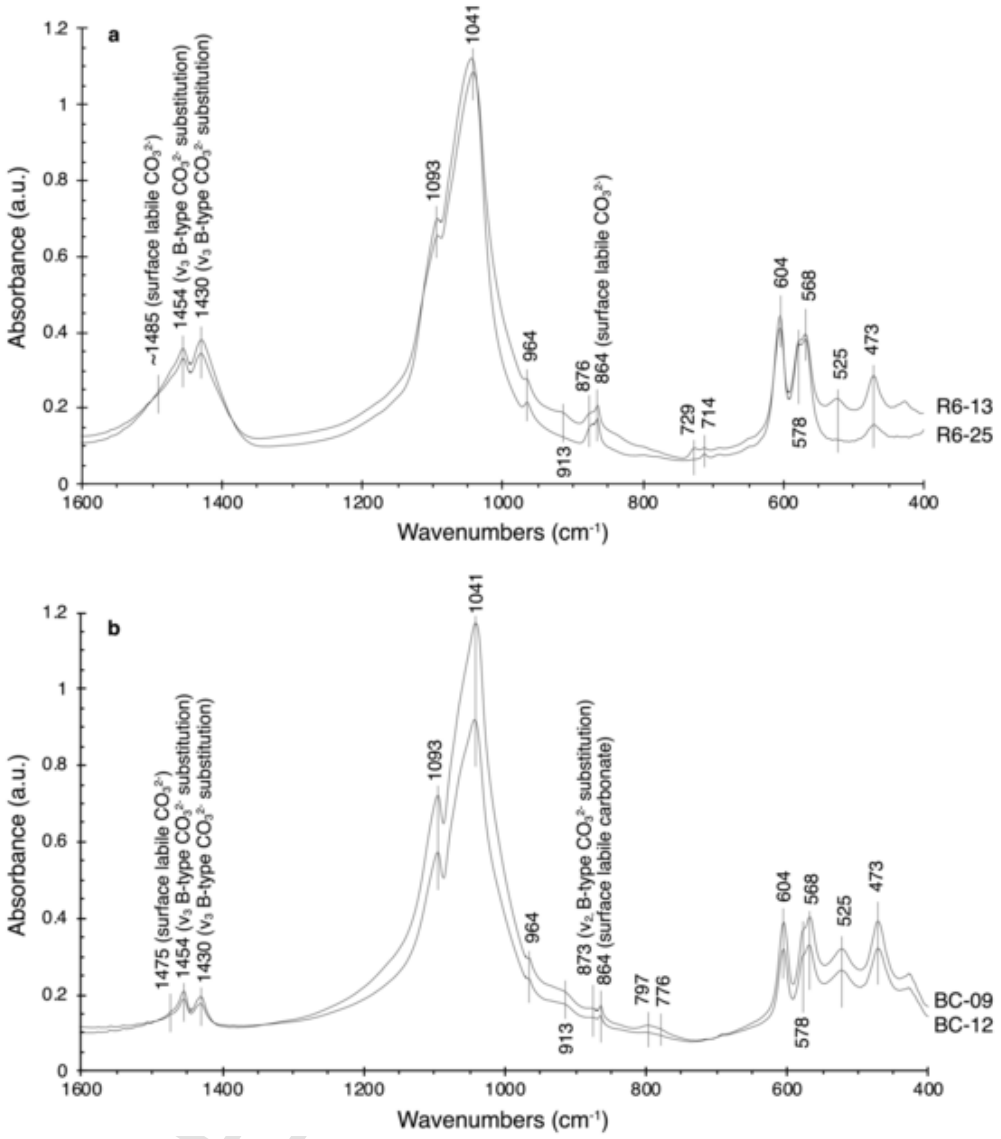

Fig. 5. FTIR spectra of representative Moroccan phosphorites. (**a**) Carbonate fluorapatite from the 6258 well, Gantour Basin. (**b**) Carbonate fluorapatite from the 1685 well, Oued Eddahab Basin. The interval from 1600 to 400 cm^{-1} highlights the four PO_4 internal vibrational modes as well as structural carbonate vibrations in phosphate minerals.

occasionally pitted with pore diameters of <2 μm (Fig. 6a-c). The examination of broken grains reveals that phosphatic peloids are composed of numerous micrometer-sized particles (Fig. 6d). At higher magnification, the crystallites frequently intersect one another and exhibit a spherical and rod-shaped morphology (Fig. 6e, f). The sphere-like microstructures are on the order of hundreds of nanometers, while the rod-shaped particles are represented by a typical length and diameter ranging from 0.9 to 1.5 μm and 0.35 to 0.5 μm, respectively. The crystallite itself is made of nanocrystallites, as suggested by the presence of fibrous-like structures (Fig. 6f, Fig. S6). Also, the investigated peloids display high porosity between crystallites (Fig. 6e, f).

Observations in BSE mode clearly show the concentrically layered texture of Gantour phosphatic coated grains, consisting of alternating light gray and dark gray laminae (Fig. 7a-c, e). It suggests changes in major element content. Moreover, the structural details of phosphatic coated grains reveal that the BSE light gray areas consist of densely packed crystallites, while nanometric intracrystalline porosity characterizes the BSE dark-gray areas (Fig. 7d, f). The latter pattern also characterizes the Oued Eddahab peloids without clear laminated structures (Fig. S7). Importantly, the occurrence of pores is not likely to explain the overall brightness change in the BSE dark-gray areas of studied Moroccan phosphates (Fig. 7d, f; Fig. S7b-d). In addition, electron distribution maps (EPMA) illustrate that the BSE light gray areas contain quantitatively higher concentrations of Ca and P than the BSE dark gray areas in the Gantour phosphatic coated grains (Fig. 8). Considering the substitution of CO_3^{2-} for PO_4^{3-} in phosphate minerals, the BSE dark gray areas should thus contain high inorganic C concentrations. Si, Na, S, and to a lesser extent K do not have the same spatial distribution as the three previous elements (Fig. 8; Fig. S8). In contrast, Fe, Cl, and F are homogeneously distributed (Fig. S8). Concentrations of Ca, P, Si, Na, and S vary as high as 4, 3, 0.8, 0.7 and 0.5 wt%, respectively. It is important to point out that porosity does not affect the chemical analyses since all elements are not depleted in the porous BSE dark gray areas (compare Ca and P with Si, Na, or S EMPA elemental maps, Fig. 8).

Table 2
EPMA analyses of selected CFA grains from the Moroccan phosphorites.

Sample	R6–29-1	R6–29-2	R6–29-3	R6–29-4	R6–30-1	R6–30-2	R6–30-3	R6–30-4	R6–30-5	R6–30-6	BC-6-1	BC-6-2	BC-6-3	BC-6-4	BC-6-5	BC-6-6	BC-6-7	BC-12-1	BC-12-2	BC-12–3	BC-12
Phosphatic allochems	CG	CG	Pel	Pel	CG	Pel	CG	Pel	CG	CG	Pel	Pel	Pel	Pel	Pel	Pel	Pel	Pel	Pel	Pel	Pel
Al_2O_3 (%)	0.00	0.12	0.02	0.10	0.03	0.08	0.13	0.06	0.10	0.33	0.17	0.09	0.10	0.16	0.23	0.08	0.09	0.21	0.04	0.22	0.15
FeO (%)	0.01	0.04	0.01	BDL	0.03	0.06	0.06	0.04	0.04	0.09	0.05	0.03	0.07	0.07	0.07	0.01	0.05	0.08	0.05	0.16	0.08
MgO (%)	0.17	0.30	0.31	0.24	0.32	0.26	0.37	0.23	0.33	0.30	0.14	0.05	0.10	0.09	0.12	0.07	0.05	0.06	0.04	0.05	0.04
CaO (%)	53.99	53.94	53.55	53.28	53.45	53.31	55.03	53.89	53.10	52.98	53.89	55.23	53.70	54.16	53.80	54.89	54.99	53.82	55.39	54.76	54.57
Na_2O (%)	0.45	0.58	0.86	0.44	0.72	0.67	0.88	0.59	0.52	0.59	0.18	0.20	0.27	0.19	0.27	0.21	0.20	0.22	0.31	0.09	0.13
K_2O (%)	0.03	0.02	0.05	0.03	0.04	0.02	0.04	0.01	0.04	0.04	0.03	0.01	0.02	0.03	0.04	0.04	0.01	0.09	0.03	0.04	0.04
P_2O_5 (%)	35.85	35.35	35.69	35.34	34.39	35.14	33.25	34.30	34.22	33.42	39.73	40.87	40.22	38.75	40.03	38.82	39.79	39.14	40.60	36.78	38.03
SO_2 (%)	0.74	0.84	0.92	0.72	0.94	0.89	0.86	0.81	0.69	0.84	0.17	0.23	0.20	0.36	0.29	0.34	0.32	0.34	0.37	0.31	0.26
SiO_2 (%)	0.11	0.47	0.13	0.56	0.08	0.35	0.27	0.21	0.60	1.13	1.96	1.45	1.65	2.22	2.66	1.53	1.19	1.37	0.24	0.80	0.53
F (wt%)	*4.43*	*4.26*	*3.81*	*4.37*	*4.21*	*4.07*	4.55	*4.41*	*4.35*	*3.98*	*4.17*	*4.00*	*4.08*	*4.07*	4.01	*4.09*	*4.18*	*3.96*	3.81	4.27	4.37
Cl (wt%)	0.05	0.02	0.05	0.02	0.09	0.04	0.07	0.06	0.07	0.06	0.01	0.00	0.02	0.00	0.01	0.01	0.02	0.08	0.10	0.03	0.03
Total	*95.84*	*95.94*	*95.39*	*95.10*	*94.29*	*94.88*	*95.50*	*94.59*	*94.07*	*93.77*	*100.48*	*101.74*	*100.44*	*100.10*	101.53	*99.64*	*100.44*	*99.37*	100.97	97.51	98.22
O = F, Cl	1.88	1.80	1.62	1.84	1.79	1.72	1.93	1.87	1.85	1.69	1.76	1.51	1.72	1.72	1.69	1.54	1.58	1.69	1.63	1.81	1.85
Corrected Total	93.97	94.14	93.78	93.26	92.50	93.16	93.57	92.72	92.22	92.08	98.72	100.23	98.71	98.39	99.84	97.91	98.68	97.69	99.35	95.70	96.37
CO_2 (%)	6.03	5.86	6.22	6.74	7.50	6.84	6.43	7.28	7.78	7.92	1.28		1.29	1.61	0.16	2.09	1.32	2.31	0.65	4.30	3.63
OH (wt%)			0.04																		
Net Corrected Total	100.00	100.00	100.04	100.00	100.00	100.00	100.00	100.00	100.00	100.00	100.00	100.23	100.00	100.00	100.00	100.00	100.00	100.00	100.00	100.00	100.0

Note: BDL = below detection limit; CG = coated grain; Pel = peloid.
Italicized numbers refer to samples for which fluorine analyses were corrected for fluorine migration (see text for explanation).

Table 3
Structural formulae of Moroccan CFA particles calculated following the stoichiometric model of Ketcham (2015).

Basin	Gantour										Oued Eddahab														
Sample	R6–29-1	R6–29-2	R6–29-3	R6–29-4	R6–30-1	R6–30-2	R6–30-3	R6–30-4	R6–30-5	R6–30-6	BC-6-1	BC-6-2	BC-6-3	BC-6-4	BC-6-5	BC-6-6	BC-6-7	BC-12-1	BC-12-2	BC-12–3	BC-12-4	BC-12-5	BC-12-6	BC-12-7	BC-12-8
Phosphatic allochems	CG	CG	Pel	Pel	CG	Pel	CG	Pel	CG	CG	Pel	Pel	Pel	Pel	Pel	Pel	Pel	Pel	Pel	Pel	Pel	Pel	Pel	Pel	Pel
Al	0.00	0.02	0.00	0.02	0.01	0.01	0.01	0.01	0.02	0.06	0.03	0.02	0.02	0.03	0.05	0.02	0.02	0.04	0.01	0.04	0.03	0.03	0.02	0.04	0.01
Fe	0.00	0.01	0.00	0.00	0.00	0.01	0.01	0.01	0.01	0.01	0.01	0.00	0.01	0.01	0.01	0.00	0.01	0.01	0.01	0.02	0.01	0.01	0.00	0.01	0.01
K	0.01	0.00	0.01	0.01	0.01	0.00	0.00	0.00	0.01	0.01	0.01	0.00	0.00	0.01	0.01	0.01	0.00	0.02	0.01	0.01	0.01	0.01	0.01	0.02	0.00
Mg	0.04	0.07	0.08	0.06	0.08	0.06	0.06	0.06	0.08	0.07	0.03	0.01	0.02	0.02	0.03	0.02	0.01	0.02	0.01	0.01	0.01	0.01	0.01	0.01	0.00
Na	0.14	0.18	0.27	0.14	0.23	0.21	0.19	0.19	0.16	0.18	0.06	0.07	0.09	0.06	0.09	0.07	0.06	0.07	0.10	0.03	0.04	0.07	0.09	0.09	0.11
Ca	9.48	9.48	9.36	9.28	9.31	9.29	9.42	9.42	9.22	9.17	9.61	9.90	9.56	9.66	9.63	9.75	9.81	9.55	9.98	9.70	9.68	9.68	9.91	9.61	9.69
∑ cationic site	9.68	9.77	9.72	9.50	9.63	9.59	9.68	9.68	9.49	9.52	9.74	10.00	9.70	9.79	9.82	9.86	9.91	9.65	10.09	9.75	9.74	9.77	10.01	9.73	9.81
Si	0.02	0.08	0.02	0.09	0.01	0.06	0.03	0.03	0.10	0.18	0.33	0.24	0.27	0.37	0.44	0.25	0.20	0.23	0.04	0.13	0.09	0.09	0.07	0.11	0.03
S	0.11	0.13	0.14	0.11	0.14	0.14	0.12	0.12	0.10	0.13	0.03	0.04	0.03	0.06	0.05	0.05	0.05	0.05	0.06	0.05	0.04	0.06	0.05	0.06	0.06
C	1.35	1.31	1.39	1.50	1.67	1.52	1.62	1.62	1.72	1.75	0.29	0.00	0.29	0.37	0.04	0.47	0.30	0.52	0.15	0.97	0.82	0.53	0.16	0.17	0.50
P	4.97	4.91	4.93	4.87	4.73	4.84	4.74	4.74	4.69	4.57	5.60	5.79	5.66	5.46	5.66	5.45	5.61	5.49	5.78	5.15	5.33	5.54	5.78	5.83	5.63
∑ anionic site	6.46	6.43	6.48	6.56	6.56	6.55	6.52	6.52	6.62	6.63	6.24	6.07	6.25	6.25	6.19	6.22	6.15	6.29	6.03	6.30	6.28	6.23	6.06	6.17	6.21
F	2.30	2.21	1.97	2.25	2.17	2.09	2.28	2.28	2.23	2.03	2.19	2.12	2.14	2.14	2.12	2.14	2.20	2.07	2.03	2.23	2.29	2.30	2.28	2.18	2.35
Cl	0.01	0.00	0.01	0.01	0.03	0.01	0.02	0.02	0.02	0.02	0.00	0.00	0.01	0.00	0.00	0.00	0.00	0.02	0.03	0.01	0.01	0.02	0.02	0.03	0.03
OH			0.02																						

Note: CG = coated grain; Pel = peloid.

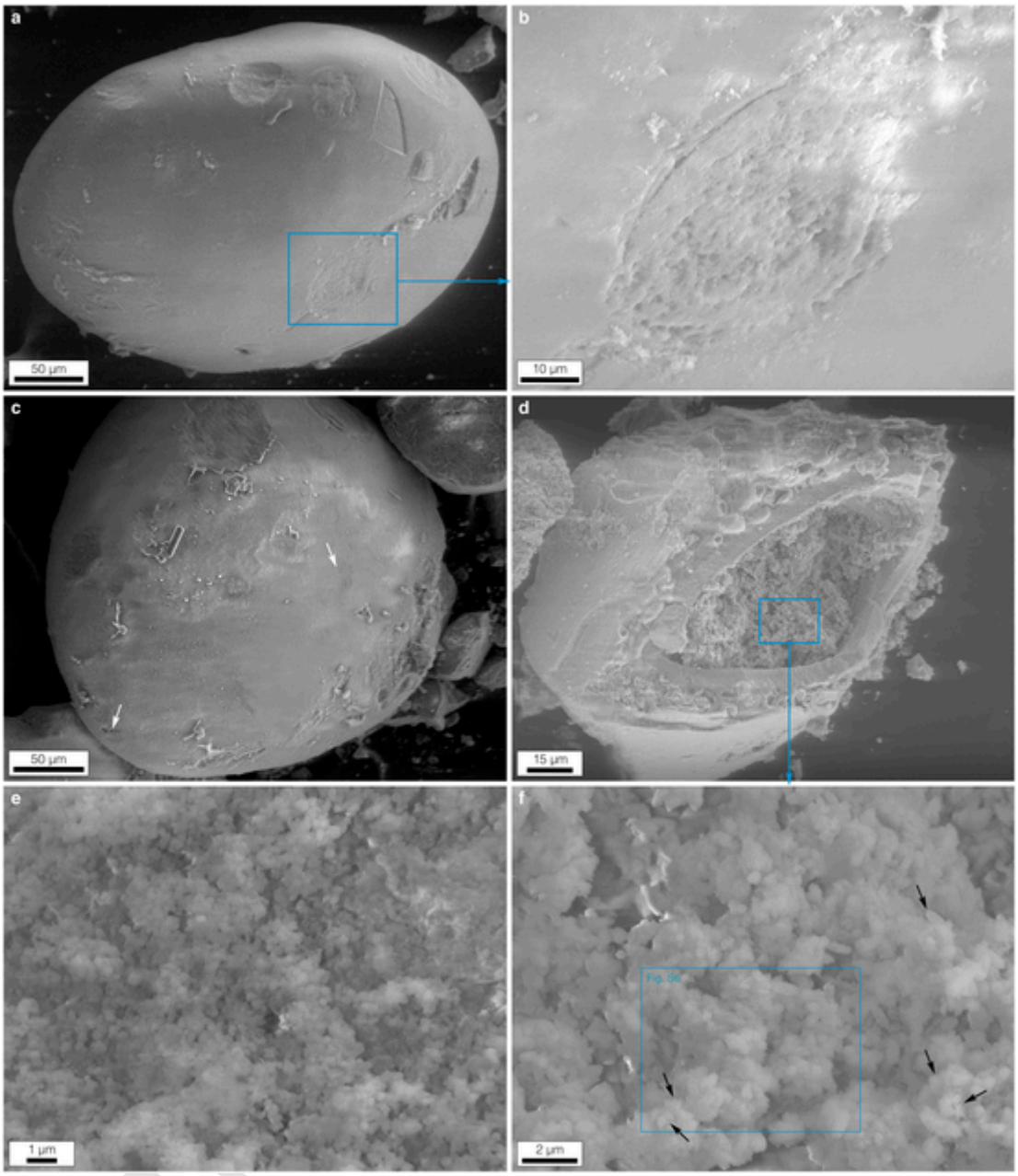

Fig. 6. SEM images in secondary electron mode of CFA peloids and crystallites from the Gantour basin. (**a**) Rounded to slightly elongated phosphatic peloid with a smooth surface that is occasionally pitted. (**b**) Close up of image a. Abundance of pores with µm-sized diameters. (**c**) Phosphatic peloid with irregular and porous surface (white arrows). (**d**) Broken phosphatic peloid composed of a large number of crystallites and high porosity. (**e**) High density of sphere-like CFA particles. (**f**) Close up of image d. Rod-shaped CFA particles that are constituted of nanocrystallites (black arrows).

5. Discussion

5.1. Origin of variable bulk CFA-hosted CO_3^{2-} concentrations

Many studies have argued that the primary causes of chemical variability in CFA were linked to weathering, diagenesis, and subsequent metamorphism (Knudsen and Gunter, 2002; McArthur, 1978; McClellan, 1980). Few works have dealt with the effect of depositional environments and/or early diagenetic processes on the CFA-hosted CO_3^{2-} content in sedimentary phosphate-bearing rocks (Glenn et al., 1988; Gulbrandsen, 1971; Nathan et al., 1990).

The studied Moroccan phosphate rocks contain remarkably heterogeneous CFA-hosted CO_3^{2-} contents at the regional scale. Notably, the Gantour CFA contain twice as much bulk CO_3^{2-} contents as the Oued Eddahab CFA (Table 1). On the other hand, a chemical homogeneity in CFA-hosted CO_3^{2-} contents is likely within each phosphate basin. Indeed, phosphatized coprolites from the Gantour and Ouled Abdoun basins show CO_3^{2-} contents varying roughly between 6 and 9%, (Cosmidis et al., 2013b; Kocsis et al., 2014), while CO_3^{2-} contents from other Oued Eddahab phosphorite deposits range from 2 to 4.72% (Nguidi et al., 2021). These values are similar to those observed in this study. Post-depositional alteration processes like weathering can alter CFA by decreasing the amount of CO_3^{2-} to form fluorapatite (McClellan and Van Kauwenbergh, 1991). Our petrographic examinations rather suggest that the preservation of concentric and irregular laminations manifests a primary origin of phosphatic grains in both the Gantour and Oued Eddahab samples. Another factor has therefore controlled the low CFA-hosted CO_3^{2-} contents in the Oued Eddahab basin. However, considering the minute size of CFA particles, we cannot completely rule out

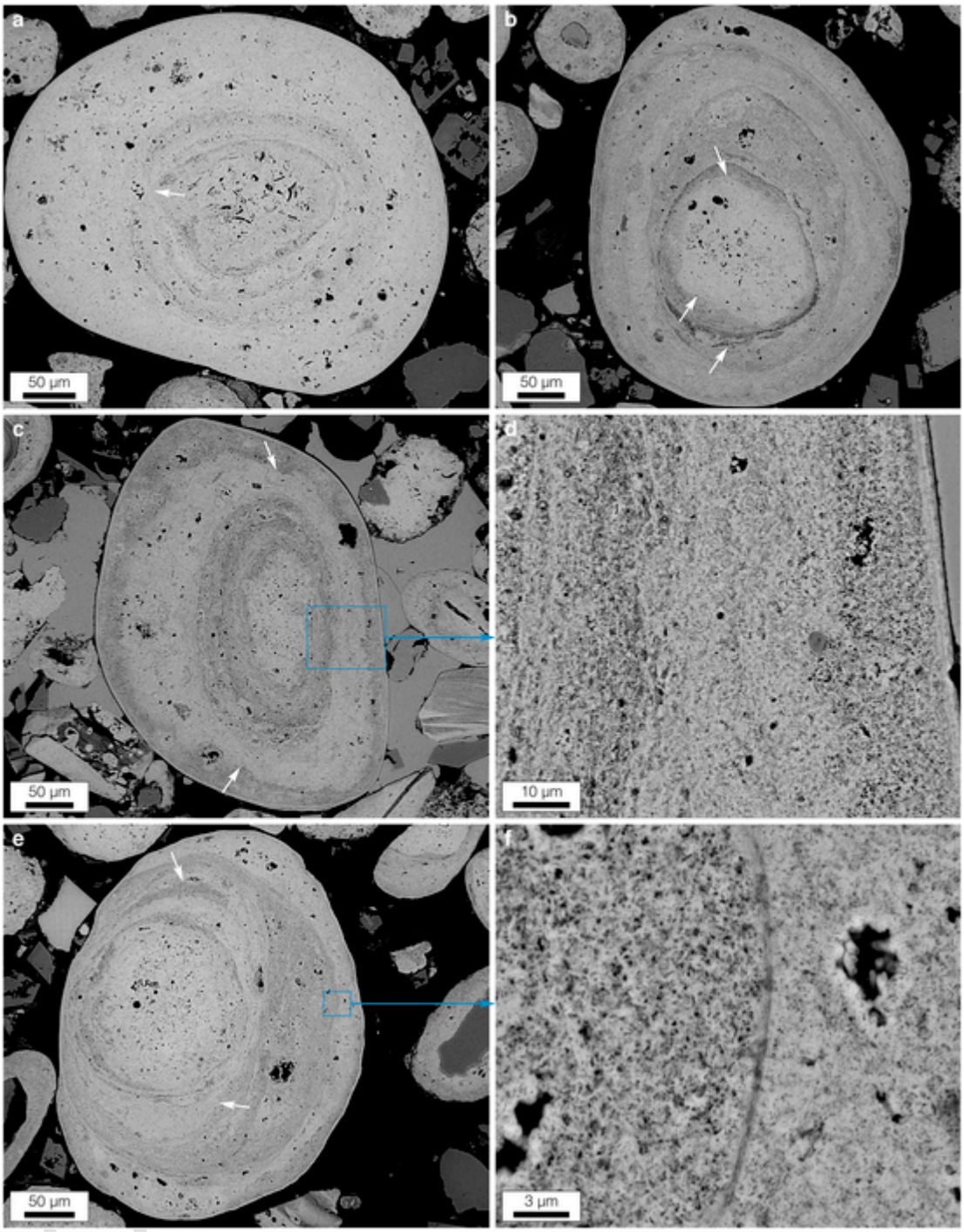

Fig. 7. SEM images in back-scattered electron mode of phosphatic coated grains from the Gantour basin. (**a-c, e**) Concentrically layered texture of alternating light gray and dark gray laminations. Most of the layers display an irregular aspect. (**d, f**). Close up of images c and e, respectively. Light gray areas exhibit densely packed crystallites, while dark gray regions host higher porosity between particles. White arrows denote the irregular and/or discontinuous aspects of laminations.

the possibility of local, low-temperature dissolution/reprecipitation or diffusion processes of few CFA crystallites during the early diagenesis.

The meaningful presence of clay material in the Oued Eddahab phosphorites compared to the Gantour phosphate deposits suggests different environmental controls. Winnowing and reworking processes through storm and bottom currents promote the enrichment of phosphatic grains to ore grade by removing fine-grained particles due to the lower density of non-phosphatic materials (1.5 to 2.5 $g.cm^{-3}$) than CFA (2.9 $g.cm^{-3}$; (Föllmi, 1996). Sea-level changes, oceanographic factors, and time contribute to winnowing intensity and exposure (El Bamiki et al., 2020; Föllmi, 1990; Pufahl and Groat, 2016). Thus, repeated hydrodynamic winnowing and reworking likely occurred in the depositional sites of Gantour basin, while less winnowed phosphates were formed within the Oued Eddahab basin. Alternatively, a large terrigenous input of clay and quartz particles could have impeded the phosphogenesis in the Oued Eddahab region as high sedimentation rate and rapid burial lowers the intensity and extent of phosphate mineralization (Filippelli, 1997). The abundance of phosphatic coated grains and broken bone fragments associated with minor amounts of fine-grained particles in the Gantour phosphorites also provide robust

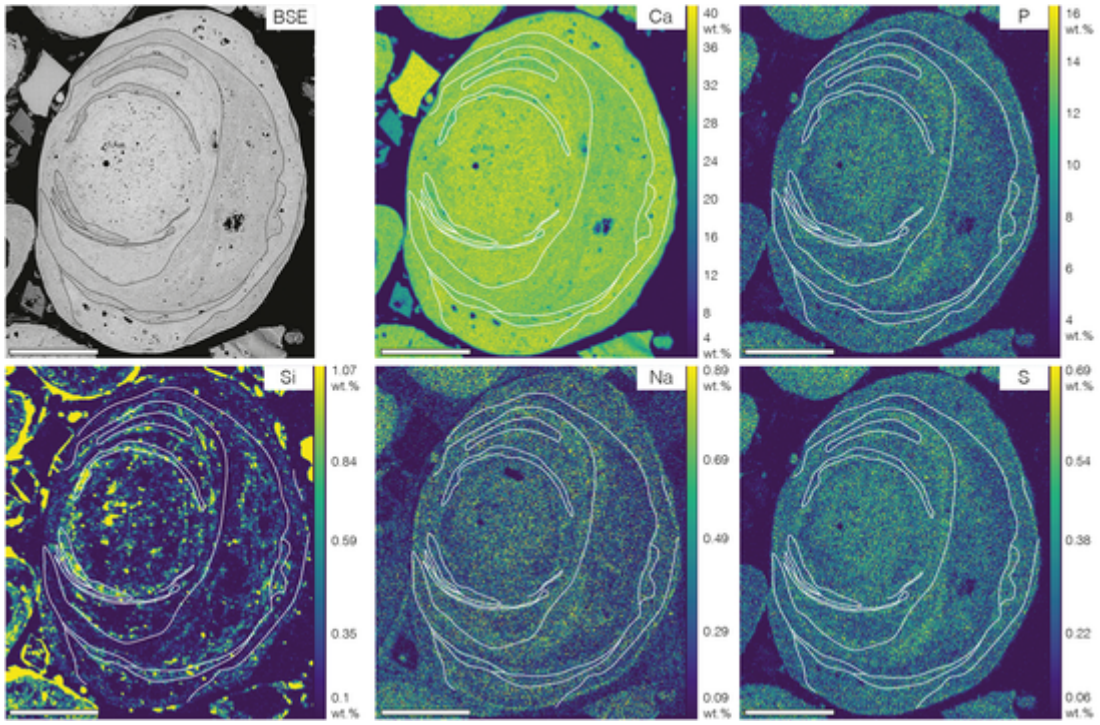

Fig. 8. SEM-BSE image of a Gantour CFA coated grain and corresponding EPMA element mapping (viridis colour map, as recommended by Stoelzle and Stein, 2021). Calcium, phosphorus, silicon, sodium, and sulfur compositional variations revealed by EMPA maps, respectively. Ca and P show a covariation, while Si, Na, and S display a distinct pattern. Black and white lines denote the main irregular concentric laminations of the coated grain. Scale bars are 100 μm.

support for high energy conditions in the depositional setting. Furthermore, irregular and discontinuous laminations of phosphatic coated grains usually witness successive stages of phosphogenesis and sediment reworking (Pufahl and Grimm, 2003). This type of lamina is widely seen in CFA grains from the Gantour basin (Figs. 2, 7). Hence, we inferred that the observed changes in petrography and mineralogy between the Moroccan phosphate basins are closely linked to distinct depositional environments. In light of these considerations, the Gantour phosphorites containing authigenic CO_3^{2-}-rich CFA would have formed under a higher energy hydrodynamic regime controlled by repetitive winnowing and reworking processes compared to the CO_3^{2-}-poor CFA from the Oued Eddahab phosphorites.

Shifts in pore water redox chemistry towards more reducing to sulfidic conditions during the coated grain formation may induce the precipitation of accessory minerals like pyrite (Pufahl and Grimm, 2003; Arning et al., 2009a). The increasing flux of organic matter at the water-sediment interface is thought to be responsible for redox variations as it conducts to increasing oxygen consumption by heterotrophic microorganisms during organic matter remineralization. This subsequently leads to an upward moving of anoxic/sulfidic zones in the sediment column. The absence of redox-dependent minerals, including glauconite and pyrite,in both the Gantour and Oued Eddahab CFA cortices does not support the establishment of intense anoxic/sulfidic, pore water conditions in the zones of CFA precipitation, which points to uniform organic carbon export and primary productivity in the surface ocean (Pufahl and Grimm, 2003; Arning et al., 2009a). Alternatively, pyrite formation may have been inhibited by a lack of iron supply in the depositional settings (Berner, 1984). Nonetheless, the latter propositions do not entirely preclude slight and local development of anoxic/sulfidic conditions in the depositional environments. Instead, the heterogeneous *in situ* CFA-hosted CO_3^{2-} content from the Gantour phosphatic coated grains and to a lesser extent in Oued Eddahab grains hint that another mechanism contributed to the chemical zonations.

The primarily composition of the two studied Moroccan basins, differing in their bioclast, clays, and CFA-hosted CO_3^{2-} contents, suggests formation of these phosphate accumulations in different depositional environments along the shallow marine platform of the eastern passive margin of the central Atlantic Ocean. The similar structural position of CO_3^{2-} in CFA between the Gantour and Oued Eddahab phosphorites, however, indicates common mechanisms for CO_3^{2-} incorporation. Carbonate apatite minerals with A-type substitutions are rarely observed in biological calcifications (bones, teeth) and natural environments (Comodi and Liu, 2000; LeGeros et al., 1969). They are usually synthesized under high-temperature and high-pressure conditions (> 950 °C and 2–4 Gpa) that are unlikely to occur in sedimentary regimes, while B-type carbonate apatites dominantly characterize the natural and low-temperature environments (Madupalli et al., 2017; Tacker, 2008). Considering the requirements of high-temperature methods to form A-type carbonate apatites, high energy barrier likely limits the A-type carbonation in sedimentary apatite minerals. The strict dominance of B-type substitution in the studied Moroccan sedimentary CFA (Fig. 5) supports the latter proposal.

5.2. CFA crystallization in the Upper Cretaceous/Paleogene phosphate series

The morphology of Moroccan CFA corresponds to rod-shaped and sphere-like particles, which is similar to the phosphatic crystallites previously studied in natural environments (Mänd et al., 2018) and laboratory experiments (Busch et al., 1999; Crosby and Bailey, 2018; Wu et al., 2010). The abiotic, experimentally generated apatite microstructures precipitated from a double-diffusion gradient using a variety of organic matrices. This could indicate that organic molecules are a prerequisite for CFA crystal growth and formation. In both laboratory experiments and modern environments, a growth continuum from rod-shaped to bulged morphology, dumbbells and spherical particles is observed (Crosby and Bailey, 2018; Mänd et al., 2018). Further investigations in the Upper Cretaceous/Paleogene phosphorites are, however, required to decipher whether the CFA crystallites form

a morphological sequence that could be directly linked to the presence of carbonaceous compounds.

Marine authigenic apatite minerals crystallize from the chemistry of the interstitial pore fluids below the water-sediment interface. The concentration of dissolved pore water PO_4^{3-} in organic-rich sediments of the upwelling zone is as high as 400 μmol.L^{-1} (Goldhammer, 2011; Krajewski et al., 1994; Schulz and Schulz, 2005). In such highly supersaturated solutions with respect to authigenic apatite, nucleation is initiated (*e.g.*, Van Cappellen and Berner, 1991). The initial degree of pore water supersaturation (with respect to apatite in this study) strongly controls the nucleation rate of the product phase (Putnis, 2009). In addition to supersaturation, amorphous calcium phosphate and octacalcium phosphate are suitable nucleation templates to lower the activation energy barrier to nucleation, which subsequently serve as precursor sites for CFA nucleation and growth (Krajewski et al., 1994; Van Cappellen and Berner, 1991). Organic extracellular polymeric substances produced by microorganisms may also act as nucleation template for the precipitation of amorphous Ca-phosphate phases (Mänd et al., 2018). Therefore, high levels of supersaturation with respect to amorphous apatite precursors coupled with a microbially mediated nucleation may explain the large number of crystals ($>10^9$ per cm^{-3}, Krajewski et al., 1994) within modern phosphorites (Mänd et al., 2018). Considering the high density of CFA crystallites in the Moroccan phosphatic grains (Fig. 6d-f; Fig. S6b-d), the above conditions of supersaturation were likely met in the Upper Cretaceous/Paleogene upwelling-related coastal sediments.

The observed divergence in CFA-hosted CO_3^{2-} content between the Moroccan phosphate basins as well as chemical zonations of Ca and P – and thus of CO_3^{2-} – in the Gantour and Oued Eddahab phosphatic coated grains could represent differences in pore water concentrations of dissolved CO_3^{2-} during CFA formation (Fig. 8, Tables 2, 3). The alternating CO_3^{2-} concentration, deduced from that of P (Fig. 8), in phosphatic coated grains often occurred after episodes of reworking and transport, as suggested by the irregular and discontinuous aspect of some laminae (Figs. 7, 8). This implies that the dissolved CO_3^{2-}-saturated solutions would have been controlled by the regional interstitial fluids of depositional setting in which the mineral growth arises. Specifically, varying rates of organic matter remineralization would have led to changes in pore water carbonate alkalinity – and thus CO_3^{2-} concentrations – below the water-sediment interface (Glenn et al., 1988). Controlled by the environmental context, we thus interpret CO_3^{2-}-enriched CFA from the Gantour phosphorites to be formed at higher pore water CO_3^{2-} concentrations compared to CO_3^{2-}-depleted CFA from Oued Eddahab phosphorites.

Earlier studies have shown that the substitution of CO_3^{2-} for PO_4^{3-} (B-type substitution) in sedimentary apatites has some effects on the unit-cell dimensions (McClellan, 1980; McClellan and Lehr, 1969; McClellan and Van Kauwenbergh, 1990). A reasonable explanation for this change of physical properties is that the trigonal-planar CO_3^{2-} substituting for a tetrahedral PO_4^{3-} causes a distortion of the crystallographic structure. The B-type CO_3^{2-} accommodation promotes a contraction and slight expansion of the *a*-cell and *c*-cell parameters of the apatite lattice, respectively (McClellan, 1980; McClellan and Lehr, 1969; McClellan and Van Kauwenbergh, 1990). Furthermore, the CO_3^{2-} substitution affects the morphology of crystallites by lowering their size and modifying their shape (Deymier et al., 2017; LeGeros et al., 1967; LeGeros, 1981). At high CO_3^{2-} concentrations, synthetic carbonate apatites are less elongated along the direction of the *c*-axis, become more equiaxial, and clearly display less defined edges and facets, which results from a lowering of the atomic order, stiffness, and surface energy (Deymier et al., 2017; LeGeros et al., 1967; LeGeros, 1981). The CO_3^{2-}-rich laminae in the Gantour phosphatic coated grains are composed of high intragranular porosity compared to the CO_3^{2-}-poor CFA laminae (Fig. 7). A siliceous amorphous phase is even locally preserved inside the Oued Eddahab phosphatic grains (Fig. 3e, f; Fig. S6), denoting the presence of important porous structures between crystallites. Combined, this could indicate an underestimated influence of CO_3^{2-} substitution on grain porosity. The general mechanism behind the formation of porous laminae might be difficult to assess with our dataset. One possible explanation for this phenomenon is that porosity developed as a result of local changes in dissolved CO_3^{2-} concentrations, resulting in variations of CFA crystallite size and shape during crystal growth. High pore water CO_3^{2-} concentrations would have promoted large incorporation of CO_3^{2-} in our studied CFA grains, reducing the crystallite size and increasing the intragranular porosity. The inverse causality (*i.e.*, where porosity induces the formation of high CO_3^{2-}-containing CFA grains) is unlikely since high rates of organic matter decomposition would have increased dissolved CO_3^{2-} and PO_4^{3-} concentrations in pore waters. It would have further led to higher levels of apatite supersaturation, in turn, resulted in higher rates of apatite precipitation (Krajewski et al., 1994), preventing the formation of porosity. Alternatively, pseudomorphism, involving dissolution-precipitation mechanisms, can generate porosity (Putnis, 2009). Indeed, mineral replacement reactions with volume reduction of the product phase may lead to an increase of porosity to balance the volume of the solid. Considering the thermodynamical metastability of CFA with respect to fluorapatite through geological time (Chien and Black, 1976; McClellan and Van Kauwenbergh, 1991), it is, however, unlikely that porous CO_3^{2-}-rich CFA replaced non-porous CO_3^{2-}-poor CFA. In this regard, we hypothesize that the small size and less defined shape of CO_3^{2-}-rich CFA crystallites could contribute to the high intracrystalline porosity in modern and ancient phosphorite-hosted CFA grains. TEM analyses of the nanostructure of CFA crystallites could affirm or refute this assumption.

5.3. New insights for phosphate rock direct application as fertilizers: open-reflections

Soluble fertilizers, such as triple superphosphate, and non-processed rock phosphate powders are used worldwide as the main P source in modern agriculture. Water-soluble fertilizers allow rapid P uptake by plants, which, in turn, boosts the short-term crop yield (Pavinato et al., 2017). They may also induce P absorption onto Fe- and Al-oxyhydroxides and clay particles, decreasing the P availability for plants. The use of soluble phosphates added with limestone can lead to greater nutrient use efficiency relative to rock phosphate powders, which is a promising technique for fertilization in specific climatic areas (Somavilla et al., 2021). Alternatively, rock phosphate powders may enable long-term P use efficiency in soils due to the low dissolution rate of apatite minerals (Pavinato et al., 2017; Szilas et al., 2007). The latter slow-release phosphatic fertilizers also favor the P recovery and recycling from agricultural runoff.

Carbonate within the apatite structure involves a strong decrease of crystallinity, thereby increasing the dissolution rate and solubility (Chien and Black, 1976; Deymier et al., 2017; LeGeros et al., 1967). CFA particles in the Gantour phosphorites typically show high bulk CO_3^{2-} content and low degree of crystallinity, as indicated by the low spacing values of (211) and (300) peaks and overlapping of (211) and (112) reflections (Table 1; Fig. 4; Fig. S4). This implies that high CO_3^{2-}-containing CFA grains from the Gantour basin are more soluble than those of the Oued Eddahab basin. Hence, the Gantour phosphate deposits in Morocco may be particularly suitable for direct use as P fertilizers. Further studies are required to decipher whether the P release from soluble CFA rock powders would be sufficient for soil fertilization. This work highlights the importance of detailed studies of phosphorites for both scientific and economic interests.

6. Conclusions

The study of the Moroccan phosphate series accumulated during the Late Cretaceous/Paleogene time interval allowed us to document the mineralogy and chemistry of phosphate deposits that were collected from two separate sedimentary basins. All studied samples clearly demonstrate the presence of carbonate fluorapatite minerals as the main P-bearing phase.

The data first indicate petrographic differences between the Gantour and Oued Eddahab phosphorites in terms of bioclast, carbonate, and clay fractions as well as CFA grain morphology, which accounts for differences in depositional environments. This would likely explain the variability of bulk CFA-hosted CO_3^{2-} content within the phosphatic peloids and coated grains orchestrated by divergent supersaturation conditions. The data further suggest that slight changes of CO_3^{2-} concentrations in sediment pore waters after winnowing, transport, and redeposition processes have locally shaped the chemistry of phosphatic coated grains. This clearly implies that stochiometric assumption of sedimentary CFA grains is not reliable. In addition, high CO_3^{2-} concentrations in CFA could have affected the grain morphology by increasing their intragranular porosity. Hence, the mineralogical and chemical diversity of the Moroccan phosphate accumulations highlights the effects of different processes and controls, including depositional physical environmental factors, post-depositional winnowing and reworking, and pore water CO_3^{2-} concentrations.

Finally, the use of naturally soluble, CO_3^{2-}-rich phosphates could ensure soil fertilization while reducing the climatic, economic and environmental impacts linked to the production and use of water-soluble triple superphosphate.

Data availability

The authors declare that the data supporting this study are available within the paper and its supplementary information files.

Uncited reference

Michard et al., 2008

Declaration of Competing Interest

The authors declare that they have no known competing financial interests or personal relationships that could have appeared to influence the work reported in this paper.

Acknowledgements

This work was funded and carried out under the scientific cooperation agreements concluded, on the one hand, between Mohammed VI Polytechnic University (UM6P) and University of Montpellier (UM) [UM6P-UM specific agreement n° UM 190775 relating to the UM6P-UM/CNRS framework agreement n° UM 190759] and, on the other hand, between OCP S.A. (OCP) and UM6P [OCP-UM6P specific agreement n° 7 "Multi-scale distribution of minor and trace elements in Moroccan phosphate deposits" relating to the OCP-UM6P framework agreement in Sciences & Technology].

Es-Said Jourani, former Director of OCP Geology, and Jamal Amalik, OCP Innovation, are warmly thanked for their constant help and support of collaborative projects between OCP, UM6P, and UM. The authors also acknowledge financial support from the European Union (ERDF) and Région Nouvelle Aquitaine. We thank Christophe Nevado and Doriane Delmas for the preparation of high-quality thin sections at UM as well as Abdelmalek Ghani and Salaheddine Chahboun for careful sample preparation for whole-rock analyses at Geo-Analytical Lab (UM6P). Bernard Fraisse and Frédéric Fernandez are thanked for their technical assistance during analytical works performed at, respectively, RRXG and MEA platforms of UM. This paper benefited from fruitful discussions with Abderrazak El Albani and Alain Meunier, IC2MP, University of Poitiers. We thank the two anonymous reviewers for their constructive comments and suggestions that have improved the manuscript.

Appendix A. Supplementary data

Supplementary data to this article can be found online at https://doi.org/10.1016/j.chemgeo.2022.120818.

References

Antonakos, A., Liarokapis, E., Leventouri, T., 2007. Micro-Raman and FTIR studies of synthetic and natural apatites. Biomaterials 28, 3043–3054. https://doi.org/10.1016/j.biomaterials.2007.02.028.

Arambourg, C., 1935. Note préliminaire sur les vertébrés fossiles des phosphates du Maroc. Bulletin de la Société Géologique de France 5, 413–440.

Arambourg, C., 1952. Les vertébrés fossiles des gisements de phosphates (Maroc-Algérie-Tunisie). Notes et Memoires du Service Geologique du Maroc 92, 1–372.

Arning, E.T., Lückge, A., Breuer, C., Gussone, N., Birgel, D., Peckmann, J., 2009a. Genesis of phosphorite crusts off Peru. Mar. Geol. 262, 68–81. https://doi.org/10.1016/j.margeo.2009.03.006.

Arning, E.T., Birgel, D., Brunner, B., Peckmann, J., 2009b. Bacterial formation of phosphatic laminites off Peru. Geobiology 7, 295–307. https://doi.org/10.1111/j.1472-4669.2009.00197.x.

Baturin, G.N., 2000. Formation and evolution of phosphorite grains and nodules on the Namibian shelf, from Recent to Pleistocene. In: Glenn, C.R., Prévôt-Lucas, L., Lucas, J. (Eds.), Marine Authigenesis: From Global to Microbial. SEPM Society for Sedimentary Geology, pp. 185–199.

Berner, R.A., 1984. Sedimentary pyrite formation: an update. Geochim. Cosmochim. Acta 48, 605–615. https://doi.org/10.1016/0016-7037(84)90089-9.

Brindley, G.W., 1980. Order-disorder in clay mineral structures. In: Crystal Structure of Clay Minerals and their X-Ray Identification. Mineralogical Society, London, pp. 125–196.

Brown, G., 1980. Associated minerals. In: Brindley, G.W., Brown, G. (Eds.), Crystal Structure of Clay Minerals and their X-Ray Identification. Mineralogical Society, London, pp. 361–410.

Burnett, W.C., 1977. Geochemistry and origin of phosphorite deposits from off Peru and Chile. Geol. Soc. Am. Bull. 88, 813–823.

Busch, S., Dolhaine, H., DuChesne, A., Heinz, S., Hochrein, O., Laeri, F., Podebrad, O., Vietze, U., Weiland, T., Kniep, R., 1999. Biomimetic morphogenesis of fluorapatite-gelatin composites: fractal growth, the question of intrinsic electric fields, core/shell assemblies, hollow spheres and reorganization of denatured collagen. Eur. J. Inorg. Chem. 1643–1653.

Cappetta, H., 1981. Additions a la faune de sélaciens fossiles du Maroc: 1: Sur la présence des genres Heptranchias, Alopias et Odontorhytis dans l'Yprésien des Ouled Abdoun. Geobios 14, 563–575. https://doi.org/10.1016/S0016-6995(81)80137-4.

Cappetta, H., Bardet, N., Pereda Suberbiola, X., Adnet, S., Akkrim, D., Amalik, M., Benabdallah, A., 2014. Marine vertebrate faunas from the Maastrichtian phosphates of Benguérir (Ganntour Basin, Morocco): Biostratigraphy, palaeobiogeography and palaeoecology. Palaeogeogr. Palaeoclimatol. Palaeoecol. 409, 217–238. https://doi.org/10.1016/j.palaeo.2014.04.020.

Chellaï, E.H., Marzoqi, M., Pascal, A., Mouflih, M., 1995. Stratigraphy and evolution of Upper Cretaceous-Palaeogene sedimentary systems in the Marrakesh High Atlas (Morocco). Comptes Rendus-Académie des Sciences de Paris Série II A 321, 745–752.

Chien, S.H., Black, C.A., 1976. Free energy of formation of carbonate apatites in some phosphate rocks. Soil Sci. Soc. Am. J. 40, 234–239. https://doi.org/10.2136/sssaj1976.03615995004000020015x.

Comodi, P., Liu, Y., 2000. CO_3 substitution in apatite: further insight from new crystal-chemical data of Kesekere (Uganda) apatite. Eur. J. Mineral. 12, 965–974.

Comodi, P., Liu, Y., Stoppa, F., Woolley, A.R., 1999. A multi-method analysis of Si-, S- and *REE* -rich apatite from a new find of kalsilite-bearing leucitite (Abruzzi, Italy). Mineral. Mag. 63, 661–672. https://doi.org/10.1180/002646199548826.

Compton, J.S., Bergh, E.W., 2016. Phosphorite deposits on the Namibian shelf. Mar. Geol. 380, 290–314. https://doi.org/10.1016/j.margeo.2016.04.006.

Cosmidis, J., Benzerara, K., Menguy, N., Arning, E., 2013a. Microscopy evidence of bacterial microfossils in phosphorite crusts of the Peruvian shelf: Implications for phosphogenesis mechanisms. Chem. Geol. 359, 10–22. https://doi.org/10.1016/j.chemgeo.2013.09.009.

Cosmidis, J., Benzerara, K., Gheerbrant, E., Estève, I., Bouya, B., Amaghzaz, M., 2013b. Nanometer-scale characterization of exceptionally preserved bacterial fossils in Paleocene phosphorites from Ouled Abdoun (Morocco). Geobiology 11, 139–153. https://doi.org/10.1111/gbi.12022.

Cox, G.M., Lyons, T.W., Mitchell, R.N., Hasterok, D., Gard, M., 2018. Linking the rise of atmospheric oxygen to growth in the continental phosphorus inventory. Earth Planet. Sci. Lett. 489, 28–36. https://doi.org/10.1016/j.epsl.2018.02.016.

Crosby, C.H., Bailey, J.V., 2018. Experimental precipitation of apatite pseudofossils resembling fossil embryos. Geobiology 16, 80–87. https://doi.org/10.1111/gbi.12264.

Deer, W.A., Howie, R.A., Zussman, J., 2013. An Introduction to the Rock-Forming

Minerals, 3rd ed. The Mineralogical Society, London.
Deymier, A.C., Nair, A.K., Depalle, B., Qin, Z., Arcot, K., Drouet, C., Yoder, C.H., Buehler, M.J., Thomopoulos, S., Genin, G.M., Pasteris, J.D., 2017. Protein-free formation of bone-like apatite: New insights into the key role of carbonation. Biomaterials 127, 75–88. https://doi.org/10.1016/j.biomaterials.2017.02.029.
Diaz, J., Ingall, E., Benitez-Nelson, C., Paterson, D., de Jonge, M.D., McNulty, I., Brandes, J.A., 2008. Marine polyphosphate: a key player in geologic phosphorus sequestration. Science 320, 652–655. https://doi.org/10.1126/science.1151751.
El Bamiki, R., 2020. Étude géologique des occurrences phosphatées du Haut-Atlas marocain : Compréhension des contrôles géologiques sur l'accumulation du phosphate. Université de Montpellier, Montpellier.
El Bamiki, R., Séranne, M., Chellaï, E.H., Merzeraud, G., Marzoqi, M., Melinte-Dobrinescu, M.C., 2020. The Moroccan High Atlas phosphate-rich sediments: unraveling the accumulation and differentiation processes. Sediment. Geol. 403, 105655. https://doi.org/10.1016/j.sedgeo.2020.105655.
El Bamiki, R., Raji, O., Ouabid, M., Elghali, A., Khadiri Yazami, O., Bodinier, J.-L., 2021. Phosphate rocks: a review of sedimentary and igneous occurrences in Morocco. Minerals 11, 1137. https://doi.org/10.3390/min11101137.
Elliott, J.C., 2002. Calcium phosphate biominerals. Rev. Mineral. Geochem. 48, 427–453. https://doi.org/10.2138/rmg.2002.48.11.
Ellouz, N., Patriat, M., Gaulier, J.-M., Bouatmani, R., Sabounji, S., 2003. From rifting to alpine inversion: mesozoic and cenozoic subsidence history of some Moroccan basins. Sediment. Geol. 156, 185–212. https://doi.org/10.1016/S0037-0738(02)00288-9.
Farmer, V.C., 1974. The Infrared Spectra of Minerals. The Mineralogical Society, London.
Filippelli, G.M., 1997. Controls on phosphorus concentration and accumulation in oceanic sediments. Mar. Geol. 139, 231–240. https://doi.org/10.1016/S0025-3227(96)00113-2.
Filippelli, G.M., 2011. Phosphate rock formation and marine phosphorus geochemistry: the deep time perspective. Chemosphere 84, 759–766. https://doi.org/10.1016/j.chemosphere.2011.02.019.
Fleet, M.E., 2009. Infrared spectra of carbonate apatites: ν2-Region bands. Biomaterials 30, 1473–1481. https://doi.org/10.1016/j.biomaterials.2008.12.007.
Föllmi, K.B., 1990. Condensation and phosphogenesis: example of the Helvetic mid-Cretaceous (northern Tethyan margin). Geol. Soc. Lond., Spec. Publ. 52, 237–252. https://doi.org/10.1144/GSL.SP.1990.052.01.17.
Föllmi, K., 1996. The phosphorus cycle, phosphogenesis and marine phosphate-rich deposits. Earth Sci. Rev. 40, 55–124. https://doi.org/10.1016/0012-8252(95)00049-6.
Frizon de Lamotte, D.F., Leturmy, P., Missenard, Y., Khomsi, S., Ruiz, G., Saddiqi, O., Guillocheau, F., Michard, A., 2009. Mesozoic and Cenozoic vertical movements in the Atlas system (Algeria, Morocco, Tunisia): an overview. Tectonophysics 475, 9–28. https://doi.org/10.1016/j.tecto.2008.10.024.
Gheerbrant, E., Sudre, J., Cappetta, H., Bignot, G., 1998. *Phosphatherium escuilliei* du Thanétien du Basin des Ouled Abdoun (Maroc), plus ancien proboscidien (Mammalia) d'Afrique. Geobios 30, 247–269.
Gheerbrant, E., Sudre, J., Cappetta, H., Mourer-Chauviré, C., Bourdon, E., Iarochene, M., Amaghzaz, M., Bouya, B., 2003. The mammal localities of Grand Daoui Quarries, Ouled Abdoun Basin, Morocco, Ypresian : a first survey. Bull. Soc. géol. Fr 174, 279–293. https://doi.org/10.2113/174.3.279.
Glenn, C.R., Arthur, M.A., Yeh, H., Burnett, W.C., 1988. Carbon isotopic composition and lattice-bound carbonate of Peru-Chile margin phosphorites. Mar. Geol. 80, 287–307.
Glenn, C.R., Föllmi, K., Riggs, S.R., Baturin, G.N., Grimm, K.A., Trappe, J., Abed, A.M., Galli-Olivier, C., Garrison, R.E., Ilyin, A.V., Jehn, C., Rohrlich, V., Sadakah, R.M.Y., Schidlowski, M., Sheldon, R.E., Siegmund, H., 1994. Phosphorus and phosphorites: sedimentology and environments of formation. Eclogae Geol. Helv. 87, 747–788, 0012-9402194/030747-42.
Goldhammer, T., 2011. Phosphate oxygen isotopes: insights into sedimentary phosphorus cycling from the Benguela upwelling system. Geochim. Cosmochim. Acta 16.
Goldhammer, T., Brüchert, V., Ferdelman, T.G., Zabel, M., 2010. Microbial sequestration of phosphorus in anoxic upwelling sediments. Nat. Geosci. 3, 557–561. https://doi.org/10.1038/ngeo913.
Goldoff, B., Webster, J.D., Harlov, D.E., 2012. Characterization of fluor-chlorapatites by electron probe microanalysis with a focus on time-dependent intensity variation of halogens. Am. Mineral. 97, 1103–1115. https://doi.org/10.2138/am.2012.3812.
Gulbrandsen, R.A., 1971. Relation of carbon dioxide content of apatite of the Phosphoria Formation to regional facies. Mountain Geol. 8, 81–84.
Hoepffner, C., Soulaimani, A., Piqué, A., 2005. The Moroccan hercynides. J. Afr. Earth Sci. 43, 144–165. https://doi.org/10.1016/j.jafrearsci.2005.09.002.
Hollard, H., Choubert, G., Bronner, G., Marchand, J., Sougy, J., 1985. Carte géologique du Maroc. Échelle 1/1 000 000.
Jahnke, R.A., 1984. The synthesis and solubility of carbonate fluorapatite. Am. J. Sci. 284, 58–78. https://doi.org/10.2475/ajs.284.1.58.
Jahnke, R.A., Emerson, S.R., Roe, K.K., Burnett, W.C., 1983. The present day formation of apatite in Mexican continental margin sediments. Geochim. Cosmochim. Acta 47, 259–266. https://doi.org/10.1016/0016-7037(83)90138-2.
Jasinski, S.M., 2020. Phosphate Rock.
Ketcham, R.A., 2015. Technical note: Calculation of stoichiometry from EMP data for apatite and other phases with mixing on monovalent anion sites. Am. Mineral. 100, 1620–1623. https://doi.org/10.2138/am-2015-5171.
Knudsen, A.C., Gunter, M.E., 2002. Sedimentary phosphorites-an example: phosphoria formation, Southeastern Idaho, U.S.A. Rev. Mineral. Geochem. 48, 363–389. https://doi.org/10.2138/rmg.2002.48.9.
Kocsis, L., Gheerbrant, E., Mouflih, M., Cappetta, H., Yans, J., Amaghzaz, M., 2014. Comprehensive stable isotope investigation of marine biogenic apatite from the late Cretaceous–early Eocene phosphate series of Morocco. Palaeogeogr. Palaeoclimatol. Palaeoecol. 394, 74–88. https://doi.org/10.1016/j.palaeo.2013.11.002.
Kocsis, L., Ulianov, A., Mouflih, M., Khaldoune, F., Gheerbrant, E., 2021. Geochemical investigation of the taphonomy, stratigraphy, and palaeoecology of the mammals from the Ouled Abdoun Basin (Paleocene-Eocene of Morocco). Palaeogeogr. Palaeoclimatol. Palaeoecol. 577, 110523. https://doi.org/10.1016/j.palaeo.2021.110523.
Krajewski, K.P., Van Cappellen, P., Trichet, J., Kuhn, O., Lucas, J., Martin-Algarra, A., Prévôt, L., Tewari, V.C., Gaspar, L., Knight, R.I., Lamboy, M., 1994. Biological processes and apatite formation in sedimentary environments. Eclogae Geol. Helv. 87, 701–745. https://doi.org/10.5169/SEALS-167475.
Labails, C., Olivet, J.-L., Aslanian, D., Roest, W.R., 2010. An alternative early opening scenario for the Central Atlantic Ocean. Earth Planet. Sci. Lett. 297, 355–368. https://doi.org/10.1016/j.epsl.2010.06.024.
LeGeros, R.Z., 1981. Apatites in biological systems. Progress in Crystal Growth and Characterization 4, 1–45. https://doi.org/10.1016/0146-3535(81)90046-0.
LeGeros, P.G., Trautz, O.R., LeGeros, J.P., Klein, E., Shirra, W.P., 1967. Apatite crystallites: effects of carbonate on morphology. Science 155, 1409–1411.
LeGeros, R.Z., Trautz, O.R., Klein, E., LeGeros, J.P., 1969. Two types of carbonate substitution in the apatite structure. Experientia 25, 5–7. https://doi.org/10.1007/BF01903856.
Lucas, J., Prévôt-Lucas, L., 1995. Tethyan Phosphates and Bioproductites. In: Nairn, A.E.M., Ricou, L.-E., Vrielynck, B., Dercourt, J. (Eds.), The Tethys Ocean. Springer, Boston, MA, pp. 367–391. https://doi.org/10.1007/978-1-4899-1558-0_12.
Lumiste, K., Mänd, K., Bailey, J., Paiste, P., Lang, L., Lepland, A., Kirsimäe, K., 2019. REE + Y uptake and diagenesis in recent sedimentary apatites. Chem. Geol. 525, 268–281. https://doi.org/10.1016/j.chemgeo.2019.07.034.
Madejová, J., Balan, E., Petit, S., 2011. Application of vibrational spectroscopy to the characterization of phyllosilicates and other industrial minerals. In: Christidis, G.E. (Ed.), Advances in the Characterization of Industrial Minerals. European Mineralogical Union, pp. 171–226. https://doi.org/10.1180/EMU-notes.9.6.
Madupalli, H., Pavan, B., Tecklenburg, M.M.J., 2017. Carbonate substitution in the mineral component of bone: discriminating the structural changes, simultaneously imposed by carbonate in A and B sites of apatite. J. Solid State Chem. 255, 27–35. https://doi.org/10.1016/j.jssc.2017.07.025.
Mänd, K., Kirsimäe, K., Lepland, A., Crosby, C.H., Bailey, J.V., Konhauser, K.O., Wirth, R., Schreiber, A., Lumiste, K., 2018. Authigenesis of biomorphic apatite particles from Benguela upwelling zone sediments off Namibia: the role of organic matter in sedimentary apatite nucleation and growth. Geobiology 16, 640–658. https://doi.org/10.1111/gbi.12309.
McArthur, J.M., 1978. Systematic variations in the contents of Na, Sr, CO_3 and SO_4 in marine carbonate-fluorapatite and their relation to weathering. Chem. Geol. 21, 89–112.
McClellan, G.H., 1980. Mineralogy of carbonate fluorapatites. J. Geol. Soc. 137, 675–681.
McClellan, G.H., Lehr, J.R., 1969. Crystal chemical investigation of natural apatites. Am. Mineral. 54, 1374–1391.
McClellan, G.H., Van Kauwenbergh, S.J., 1990. Mineralogy of sedimentary apatites. Geol. Soc. Lond., Spec. Publ. 52, 22–31. https://doi.org/10.1144/GSL.SP.1990.052.01.03.
McClellan, G.H., Van Kauwenbergh, S.J., 1991. Mineralogical and chemical variation of francolites with geological time. J. Geol. Soc. 148, 809–812. https://doi.org/10.1144/gsjgs.148.5.0809.
Michard, A., Frizon de Lamotte, D., Saddiqi, O., Chalouan, A., 2008. An outline of the geology of Morocco. In: Michard, André, Saddiqi, Omar, Chalouan, Ahmed, de Lamotte, Frizon, Dominique (Eds.), Continental Evolution: The Geology of Morocco, Lecture Notes in Earth Sciences. Springer, Berlin, Heidelberg, pp. 1–31. https://doi.org/10.1007/978-3-540-77076-3_1.
Mouflih, M., 2015. Les phosphates du Maroc central et du Moyen Atlas (Maastrichtien-Lutetien, Maroc): Sedimentologie, stratigraphie sequentielle, contexte genetique et valorisation. Université de Cadi Ayyad, Marrakech.
Nathan, Y., 1984. The Mineralogy and Geochemistry of Phosphorites. In: Nriagu, J.O., Moore, P.B. (Eds.), Phosphate Minerals. Springer-Verlag, Berlin, Heidelberg, pp. 275–291.
Nathan, Y., 1996. Mechanism of CO_2^{-3} substitution in carbonate-fluorapatite; evidence from FTIR spectroscopy, ^{13}C NMR, and quantum mechanical calculations - Discussion. Am. Mineral. 81, 513–514. https://doi.org/10.2138/am-1996-3-425.
Nathan, Y., Soudry, D., Avigour, A., 1990. Geological significance of carbonate substitution in apatites: Israeli phosphorites as an example. Geol. Soc. Lond., Spec. Publ. 52, 179–191. https://doi.org/10.1144/GSL.SP.1990.052.01.13.
Nguidi, M.A., Mouflih, M., Benbouziane, A., Kocsis, L., El Ouariti, S., El Boukhari, H., Aquit, M., Yazami, O.K., 2021. Lithofacies analysis, sedimentary dynamics and genesis of Maastrichtian-Eocene phosphorites of BouCraa deposit (Southern Morocco). J. Afr. Earth Sci. 177, 104161. https://doi.org/10.1016/j.jafrearsci.2021.104161.
Noubhani, A., Cappetta, H., 1994. Révision des Rhombodontidae (Neoselachii, Batomorphii) des bassins à phosphate du Maroc. Palaeovertebrata 23, 1–49.
Ollivier-Pierre, M.-F., 1982. La microflore du Paléocène et de l'Eocène des séries phosphatées des Ganntour (Maroc). Sci. Géol. Bull. 35, 117–127. https://doi.org/10.3406/sgeol.1982.1615.
Pavinato, P.S., Rodrigues, M., Soltangheisi, A., Sartor, L.R., Withers, P.J.A., 2017. Effects of cover crops and phosphorus sources on maize yield, phosphorus uptake, and phosphorus use efficiency. Agron. J. 109, 1039–1047. https://doi.org/10.2134/agronj2016.06.0323.
Piqué, A., Ait Brahim, L., Ait Ouali, R., Amrhar, M., Charroud, M., Gourmelen, C., Laville, E., Rekhiss, F., Tricart, P., 1998. Structural evolution of the Maghreb Atlasic domains during Mesozoic and Cenozoic times. The role of inherited structures during the deformation of the North African margin. Bulletin de la Société Géologique de France 169, 797–810.
Prévôt, L., 1988. Geochimie et petrographie de la formation à phosphate des Ganntour

(Maroc): Utilisation pour une explication de la genèse des phosphorites Crétacé-Eocènes. Université Louis Pasteur, Strasbourg.
Pufahl, P.K., Grimm, K.A., 2003. Coated phosphate grains: proxy for physical, chemical, and ecological changes in seawater. Geol 31, 801–804. https://doi.org/10.1130/G19658.1.
Pufahl, P.K., Groat, L.A., 2016. Sedimentary and igneous phosphate deposits: formation and exploration: an invited paper. Econ. Geol. 112, 483–516. https://doi.org/10.2113/econgeo.112.3.483.
Putnis, A., 2009. Mineral replacement reactions. Rev. Mineral. Geochem. 70, 87–124. https://doi.org/10.2138/rmg.2009.70.3.
Ranke, U., von Rad, U., Wissmann, G., 1982. Stratigraphy, facies and tectonic development of the on- and offshore Aaiun-Tarfaya Basin — a review. In: von Rad, U., Hinz, K., Sarnthein, M., Seibold, E. (Eds.), Geology of the Northwest African Continental Margin. Springer, Berlin, Heidelberg, pp. 86–105. https://doi.org/10.1007/978-3-642-68409-8_6.
Rauscher, R., Doubinger, J., 1982. Les dinokystes du Maestrichtien phosphaté du Maroc. Sci. Géol. Bull. 35, 97–116. https://doi.org/10.3406/sgeol.1982.1614.
Regnier, P., Lasaga, A.C., Berner, R.A., Han, O.H., Zilm, K.W., 1994. Mechanism of CO_3^{2-} substitution in carbonate-fluorapatite: evidence from FTIR spectroscopy, ^{13}C NMR, and quantum mechanical calculations. Am. Mineral. 79, 809–818.
Reinhard, C.T., Planavsky, N.J., Gill, B.C., Ozaki, K., Robbins, L.J., Lyons, T.W., Fischer, W.W., Wang, C., Cole, D.B., Konhauser, K.O., 2017. Evolution of the global phosphorus cycle. Nature 541, 386–389. https://doi.org/10.1038/nature20772.
Ruttenberg, K.C., 2003. The global phosphorus cycle. In: Schlesinger, W.H. (Ed.), Treatise on Geochemistry, Vol. 8. Elsevier Ltd, pp. 585–643.
Ruttenberg, K.C., Berner, R.A., 1993. Authigenic apatite formation and burial in sediments from non-upwelling, continental margin environments. Geochim. Cosmochim. Acta 57, 991–1007. https://doi.org/10.1016/0016-7037(93)90035-U.
Salvan, H., 1954. Les invertébrés fossiles des phosphates marocains. Notes et Memoires du Service Geologique du Maroc 93, 1–258.
Schenau, S.J., Slomp, C.P., De Lange, G.J., 2000. Phosphogenesis and active phosphorite formation in sediments from the Arabian Sea oxygen minimum zone. Mar. Geol. 169, 1–20. https://doi.org/10.1016/S0025-3227(00)00083-9.
Schuffert, J.D., Kastner, M., Emanuele, G., Jahnke, R.A., 1990. Carbonate-ion substitution in francolite: a new equation. Geochim. Cosmochim. Acta 54, 2323–2328. https://doi.org/10.1016/0016-7037(90)90058-S.
Schuffert, J.D., Jahnke, R.A., Kastner, M., Leather, J., Sturz, A., Wing, M.R., 1994. Rates of formation of modern phosphorite off western Mexico. Geochim. Cosmochim. Acta 58, 5001–5010. https://doi.org/10.1016/0016-7037(94)90227-5.
Schulz, H.N., Schulz, H.D., 2005. Large sulfur bacteria and the formation of phosphorite. Science 307, 416–418. https://doi.org/10.1126/science.1103096.
Somavilla, A., Caner, L., Bortoluzzi, E.C., Santanna, M.A., Rheinheimer dos Santos, D., 2021. P-legacy effect of soluble fertilizer added with limestone and phosphate rock on grassland soil in subtropical climate region. Soil Tillage Res. 211, 105021. https://doi.org/10.1016/j.still.2021.105021.
Stock, M.J., Humphreys, M.C.S., Smith, V.C., Johnson, R.D., Pyle, D.M., EIMF, 2015. New constraints on electron-beam induced halogen migration in apatite. Am. Mineral. 100, 281–293. https://doi.org/10.2138/am-2015-4949.
Stoelzle, M., Stein, L., 2021. Rainbow color map distorts and misleads research in hydrology – guidance for better visualizations and science communication. Hydrol. Earth Syst. Sci. 25, 4549–4565. https://doi.org/10.5194/hess-25-4549-2021.
Stormer, J.C., Pierson, M.L., Tacker, R.C., 1993. Variation of F and Cl X-ray intensity due to anisotropic diffusion in apatite during electron microprobe analysis. Am. Mineral. 78, 641–648.
Szilas, C., Semoka, J.M.R., Borggaard, O.K., 2007. Can local Minjingu phosphate rock replace superphosphate on acid soils in Tanzania? Nutr. Cycl. Agroecosyst. 77, 257–268. https://doi.org/10.1007/s10705-006-9064-4.
Tacker, R.C., 2008. Carbonate in igneous and metamorphic fluorapatite: two type a and two type B substitutions. Am. Mineral. 93, 168–176. https://doi.org/10.2138/am.2008.2551.
Van Cappellen, P., Berner, R.A., 1991. Fluorapatite crystal growth from modified seawater solutions. Geochim. Cosmochim. Acta 55, 1219–1234. https://doi.org/10.1016/0016-7037(91)90302-L.
Wu, Y.-J., Tseng, Y.-H., Chan, J.C.C., 2010. Morphology control of fluorapatite crystallites by citrate ions. Cryst. Growth Des. 10, 4240–4242. https://doi.org/10.1021/cg100859m.
Yans, J., Amaghzaz, M., Bouya, B., Cappetta, H., Iacumin, P., Kocsis, L., Mouflih, M., Selloum, O., Sen, S., Storme, J.-Y., Gheerbrant, E., 2014. First carbon isotope chemostratigraphy of the Ouled Abdoun phosphate Basin, Morocco; implications for dating and evolution of earliest African placental mammals. Gondwana Res. 25, 257–269. https://doi.org/10.1016/j.gr.2013.04.004.
Zwicker, J., Smrzka, D., Steindl, F., Böttcher, M.E., Libowitzky, E., Kiel, S., Peckmann, J., 2021. Mineral authigenesis within chemosynthetic microbial mats: coated grain formation and phosphogenesis at a cretaceous hydrocarbon seep, New Zealand. Depositional Record 7, 294–310.